Radiative–Convective Equilibrium over an Idealized Land Surface with Fixed Soil Moisture

LOIS I. TANG[a] AND KAIGHIN A. MCCOLL[a,b]

[a] *Department of Earth and Planetary Sciences, Harvard University, Cambridge, Massachusetts*
[b] *School of Engineering and Applied Sciences, Harvard University, Cambridge, Massachusetts*

(Manuscript received 26 August 2024, in final form 26 August 2025, accepted 11 September 2025)

ABSTRACT: Radiative–convective equilibrium (RCE) is an idealized model of the atmosphere in which surface fluxes exactly balance radiative cooling. While recent work has shown RCE over land is a reasonable first-order model of continental climate, previous RCE studies have mainly focused on ocean surfaces. Unlike the ocean, the land surface has limited water and a low heat capacity. Here, we use theory and simulations to understand RCE over an idealized land surface with fixed soil moisture, a logical next step in the land climate model hierarchy. The fixed soil moisture case is also relevant to irrigated areas, groundwater-fed ecosystems, and broader debates about potential evapotranspiration (PET), aridity, and their changes in a warming world. We derive a parsimonious gray gas theory that reproduces major aspects of cloud-permitting simulations of RCE over an idealized land surface and permits analytic solutions for several special cases. Over fixed dry surfaces, the theory shows that hydrological sensitivity follows Clausius–Clapeyron scaling, considerably greater than the typical 2%–3% K^{-1} over oceans. Over fixed saturated surfaces, the theory reconciles divergent explanations for hydrological sensitivity based on surface and atmospheric energy budgets, with changes in near-surface relative humidity playing a key role. Finally, the theory shows that PET primarily scales with surface net radiation, rather than temperature or vapor pressure deficit, in agreement with recent empirical findings. The predicted PET scaling implies only modest changes in global mean aridity with warming, rather than the large increases implied by some prior studies. Biological plant responses to increasing carbon dioxide (CO_2) are not essential to this explanation.

SIGNIFICANCE STATEMENT: Will global warming make the world more arid? There has been a lot of debate on this question, with some arguing it will drastically increase aridity. Answering it requires understanding changes in atmospheric water demand: the evapotranspiration that would occur if the land surface was always kept saturated. We use basic physics to understand climate over land surfaces in which soils are kept saturated—and, more broadly, fixed at any level of saturation, from wet to dry. Our results support the view that global warming will not drastically increase aridity, on average. We also show that rainfall increases with warming at a faster rate over fixed dry land surfaces than it does on Earth (where land surfaces change from dry to wet and back again).

KEYWORDS: Climate; Radiative-convective equilibrium; Hydrologic cycle; Soil moisture

1. Introduction

Radiative–convective equilibrium (RCE) is an idealized state in which surface heat fluxes balance atmospheric radiative cooling, on average (Manabe and Strickler 1964; Manabe and Wetherald 1967). While only strictly valid in the global mean, it has become a widely celebrated idealization (e.g., Jeevanjee et al. 2022) that is central to our understanding of Earth's climate (Manabe and Wetherald 1967; Ramanathan and Coakley 1978). It has also proven a useful idealization for understanding various aspects of tropical climate. However, its utility beyond the tropics is less well appreciated. Miyawaki et al. (2022) recently demonstrated the approximate validity of an RCE-like regime (which includes cases in which atmospheric moist static energy flux divergence contributes significantly to cooling the column, unlike classical RCE) as far as 40°N in the zonal and annual mean. They attribute this result to the presence of land. This suggests that RCE may provide at least some first-order understanding of large-scale midlatitude continental regions, too (see section 2g for further discussion on this point).

In this study, we consider RCE over an idealized inland continental region with essentially fixed soil moisture (more precisely, soil moisture is relaxed to a fixed value on a time scale of 1 day). Why fix soil moisture? While most land on Earth does not have fixed soil moisture, it is the logical next step in the model hierarchy (Held 2005; Jeevanjee et al. 2017; Maher et al. 2019), analogous to fixing surface temperatures. Almost all previous cloud-permitting studies have focused on RCE over an ocean surface [while studies that parameterize convection have provided useful insights (Rochetin et al. 2014; Becker and Stevens 2014; Zhou et al. 2023), our focus here is on studies that resolve it]. Over ocean, the surface is saturated and its temperature is often treated as fixed (e.g., Tompkins and Craig 1998; Bretherton et al. 2005). In contrast, land can dry out, and its temperature is not fixed: It responds interactively to radiative forcing, due to its much lower heat capacity. Cronin and Chavas (2019) simulated a dry surface in RCE, but surface temperatures remained fixed. Several studies allowed surface

Denotes content that is immediately available upon publication as open access.

Corresponding authors: Lois I. Tang, loistang@fas.harvard.edu; Kaighin A. McColl, kmccoll@seas.harvard.edu

DOI: 10.1175/JCLI-D-24-0438.1

temperatures to vary interactively but retained a saturated surface (Cronin et al. 2015; Hohenegger and Stevens 2016; Tan et al. 2016; Schneider et al. 2019). Others have explored RCE over land with interactive soil moisture in a few special cases. Leutwyler and Hohenegger (2021) simulated RCE over a tropical island, whereas our focus is on inland continental regions where sea-breeze effects are insubstantial. Hohenegger and Stevens (2018) conducted cloud-permitting simulations of RCE over an idealized land surface with interactive soil moisture. Our study differs from their work in several respects, including by conducting a wider range of RCE simulations with varied top-of-atmosphere (TOA) insolation, and in deriving a simple theory to explain our results over a wide range of climates. Our work also differs from Cheng et al. (2021), who conducted a suite of RCE simulations over a land surface. That work focused on transient soil moisture–precipitation feedbacks, whereas our study addresses the equilibrium state.

Of particular relevance to the fixed soil moisture case is the fate of potential evapotranspiration (PET) in a warming world. PET is the evapotranspiration rate that would occur over a land surface if it was saturated (or, more generally, not constrained by land surface water limitation). Some of the most common arguments about the fate of the water cycle in a warming world are based on changes in the ratio PET/P (the "aridity index"), where P is the precipitation. Ambiguity in the definition of PET results in profoundly different aridity projections in future climates, depending on which definition of PET is used. If PET is assumed to largely scale with saturation vapor pressure deficit, then both theory (Sherwood and Fu 2014) and models (Scheff and Frierson 2014, 2015) project significant drying of land surfaces in a warmer world. On the other hand, if PET is assumed to largely scale with surface net radiation (Budyko 1958; Milly and Dunne 2016), then there is essentially no discernible change in aridity with warming, on average (Greve et al. 2019). Which scaling for PET is correct? Answering this question requires understanding climates in which soil moisture is fixed.

A common objection to fixing soil moisture is the claim that water is no longer conserved. For example, in an environment with low precipitation and high evapotranspiration rates, fixing soil moisture at a high value implicitly requires an additional, seemingly artificial water source for water to remain conserved. However, essentially saturated soils naturally arise in otherwise dry landscapes on Earth in the current climate, implying there is nothing artificial about this scenario. A prominent example is the Qattara Depression in the Sahara Desert, which includes perennially wet marshes, salt pans, and even lakes, despite very low rainfall (Ball 1933; Embabi 2018). Water is supplied by massive groundwater aquifers that filled during wetter past climates (Voss and Soliman 2014). More generally, the Qattara Depression is an example of a groundwater-dependent ecosystem (Laio et al. 2009; Tamea et al. 2009; Rohde et al. 2024), for which soil water storage is essentially fixed at a high value in an otherwise dry environment. Groundwater-dependent ecosystems are present in at least one-third of global drylands (Rohde et al. 2024). In addition, large parts of the central United States, India, and the North China Plain are irrigated using groundwater. The aim of irrigation is to essentially fix soil moisture at a relatively high value, at least during the growing season.

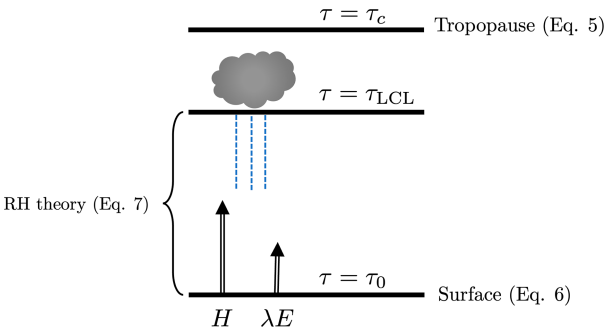

FIG. 1. Schematic overview of the theory. The theory consists of three governing equations: energy balance at the tropopause [Eq. (5)], energy balance at the surface [Eq. (6)], and an equation [Eq. (7)] based on a recent theory of near-surface RH over land (McColl and Tang 2024) that conceptually corresponds to energy balance below the LCL. The three governing equations are used to solve for three unknowns: surface temperature (T_s), near-surface air temperature (T_a), and near-surface RH. The vertical coordinate shown here is the optical depth (τ), with specific values shown for the surface (τ_0), LCL (τ_{LCL}), and tropopause (τ_c). The surface sensible (H) and latent (λE) heat fluxes are also shown.

At the opposite extreme, in an environment with high precipitation and low evapotranspiration rates, fixing soil moisture at a low value implicitly requires an additional, seemingly artificial water sink for water to remain conserved. Again, there is nothing necessarily artificial about this scenario: For example, soil moisture is approximately fixed at a relatively low value in rocky or urban environments where water drains efficiently from the surface to groundwater reservoirs (Chen et al. 2022) or engineered drainage systems. In short, there is nothing unphysical about fixing soil moisture at either high or low values, since groundwater reservoirs can (and, in many places, do) act as a source or sink to close the water budget.

This manuscript is structured as follows. In section 2, we derive a simple theory for RCE over land and discuss its assumptions and limitations. In section 3, the theory is evaluated using a suite of cloud-permitting simulations spanning a wide range of climates. In section 4, we consider a special case of the theory that permits analytic solutions. The analytic theory is then used to answer several basic questions about hydrological sensitivity over land and ocean (section 5) and to address the debate about how aridity should be expected to change in a warming world (section 6). We conclude with a summary and an outline of possible future applications in section 7.

2. Theory

a. Overview

Our theory extends the work of Robinson and Catling (2012) to include a land surface and a hydrologic cycle (Fig. 1). It has three governing equations: 1) energy balance at the tropopause [Eq. (5)], 2) energy balance at the land surface [Eq. (6)], and 3) an equation based on a recent theory of relative humidity (McColl and Tang 2024) that approximately corresponds to energy balance below the lifting condensation level [LCL;

Eq. (7)]. These three equations are used to solve for three unknowns: surface temperature (T_s), near-surface air temperature (T_a), and near-surface relative humidity (RH). There are 10 parameters (discussed in further detail below): the surface emissivity (ϵ_s), the optical depth at the surface (τ_0) and at the tropopause (τ_c), a parameter relating optical depth to pressure (n), the bulk atmospheric lapse rate (β), net shortwave radiation at the surface [$F_*^{\text{net}}(\tau_0)$] and at the tropopause [$F_*^{\text{net}}(\tau_c)$], downwelling longwave radiation at the tropopause (F_c^-), surface aerodynamic conductance (g_a), and surface conductance to water vapor (g_s). As we will show, the theory is not particularly sensitive to some of these parameters. In section 4, we consider a simpler version of the model that only requires four parameters [τ_0, n, β, and $F_*^{\text{net}}(\tau_0)$].

b. Vertical profiles of optical depth and temperature

As in Robinson and Catling (2012), we assume gray radiative transfer. Following Robinson and Catling (2012), the gray thermal optical depth τ is related to atmospheric pressure by the relation:

$$\tau = \tau_0 \left(\frac{p}{p_0}\right)^n, \tag{1}$$

where p is the atmospheric pressure, τ_0 is the gray infrared optical depth integrated down from the TOA to the reference pressure level p_0, and n is a fitted parameter that typically lies between 1 and 4 (O'Gorman and Schneider 2008; Beucler and Cronin 2016).

Using the same approach as in Robinson and Catling (2012), the temperature profile T between the surface and the tropopause is

$$T = T_a \left(\frac{p}{p_0}\right)^\beta, \tag{2}$$

where T_a is the near-surface air temperature and β is the bulk atmospheric lapse rate, which is treated as an external parameter in their simple model. For a dry adiabat, $\beta = (c_p - c_v)/c_p$, where c_p and c_v are the specific heat capacities of air at constant pressure and constant volume, respectively (using typical values on Earth, this implies $\beta \approx 0.29$ for a dry adiabat). However, in RCE, the temperature profile is typically closer to a moist adiabatic lapse rate, for which β is temperature dependent and lower, with typical values in the range of 0.18–0.22. Like Robinson and Catling (2012), β is treated as a fixed parameter, rather than internally determined, in our theory. We could have instead used an exact or approximate expression for β that includes temperature dependence instead of prescribing it as a fixed parameter, but this greatly complicates the theory. We discuss this limitation further at the end of this section.

In contrast to Robinson and Catling (2012), we do not explicitly model the stratosphere, consistent with similar previous studies (Pierrehumbert 2010). While our focus is on the troposphere, we do allow for stratospheric contributions to the troposphere through the parameter F_c^-; however, it has a generally small impact on our results.

c. Gray gas longwave radiative transfer

We employ a gray radiative transfer scheme for longwave radiation, as in Robinson and Catling (2012). The two-stream Schwarzschild equations for the upwelling and downwelling longwave radiative fluxes (F^+ and F^-, respectively) in a one-dimensional, plane-parallel, and gray atmosphere are (e.g., Pierrehumbert 2010) as follows:

$$\frac{dF^+}{d\tau} = D[F^+(\tau) - \sigma T(\tau)^4],$$

$$\frac{dF^-}{d\tau} = -D[F^-(\tau) - \sigma T(\tau)^4],$$

where $\sigma = 5.67 \times 10^{-8}$ W (m^2 K^4)$^{-1}$ is the Stefan–Boltzmann constant and $D \approx 1.66$ is the diffusivity factor. These two equations can be solved by substituting in Eqs. (1) and (2) and applying two boundary conditions. The first boundary condition is the upwelling longwave radiative flux at the surface: $F^+(\tau_0) = \epsilon_s \sigma T_s^4$, where ϵ_s is the emissivity of the land surface and T_s is the land surface temperature, which differs from the near-surface air temperature T_a. The second boundary condition is the downwelling longwave radiative flux at the tropopause: $F^-(\tau_c) \equiv F_c^-$, where F_c^- is the imposed value and τ_c is the height of the tropopause in optical depth coordinates. The resulting solutions are

$$F^+(\tau) = \epsilon_s \sigma T_s^4 e^{-D(\tau_0 - \tau)} + D\sigma T_a^4 \int_\tau^{\tau_0} \left(\frac{\tau'}{\tau_0}\right)^{(4\beta)/n} e^{-D(\tau' - \tau)} d\tau', \tag{3}$$

$$F^-(\tau) = F_c^- e^{-D(\tau - \tau_c)} + D\sigma T_a^4 \int_{\tau_c}^{\tau} \left(\frac{\tau'}{\tau_0}\right)^{(4\beta)/n} e^{-D(\tau - \tau')} d\tau'. \tag{4}$$

These equations are similar to Eqs. (12) and (14) in Robinson and Catling (2012). Differences arise because, unlike Robinson and Catling (2012), we do not require that the land surface temperature and near-surface air temperature remain identical.

d. Tropopause energy balance

At the tropopause, net shortwave radiation is balanced by net longwave radiation:

$$\begin{aligned} F_*^{\text{net}}(\tau_c) &= F^+(\tau_c) - F^-(\tau_c) \\ &= \epsilon_s \sigma T_s^4 e^{-D(\tau_0 - \tau_c)} + D\sigma T_a^4 \int_{\tau_c}^{\tau_0} \left(\frac{\tau'}{\tau_0}\right)^{(4\beta)/n} e^{-D(\tau' - \tau_c)} d\tau' - F_c^-, \end{aligned} \tag{5}$$

where $F_*^{\text{net}}(\tau_c) = F_*^+(\tau_c) - F_*^-(\tau_c)$ is the net shortwave radiation at the tropopause, with F_*^+ and F_*^- being the shortwave equivalents of F^+ and F^-.

e. Surface energy balance

Unlike Robinson and Catling (2012), we also include a surface energy balance. At the surface, latent and sensible heat fluxes balance net shortwave and longwave radiation:

$$\overbrace{\rho c_p g_a (T_s - T_a)}^{H} + \overbrace{\rho\lambda \frac{g_s g_a}{g_s + g_a}[q^*(T_s) - \mathrm{RH} q^*(T_a)]}^{\lambda E} = \underbrace{F_*^{\mathrm{net}}(\tau_0) - \epsilon_s \sigma T_s^4 + F_c^- e^{-D(\tau_0 - \tau_c)} + D\sigma T_a^4 \int_{\tau_c}^{\tau_0} \left(\frac{\tau'}{\tau_0}\right)^{(4\beta)/n} e^{-D(\tau_0 - \tau')} d\tau'}_{R_n}, \quad (6)$$

where ρ is the density of air, c_p is the specific heat capacity of air at constant pressure, λ is the latent heat of vaporization, g_a is the aerodynamic conductance (a parameter controlling near-surface turbulent mixing, often parameterized as the product of a drag coefficient and wind speed), g_s is the surface conductance (a parameter controlling surface water limitation), $q^*(T)$ is the saturation specific humidity at temperature T, and RH is the near-surface relative humidity. For a completely dry surface, $g_s = 0$; for a completely saturated surface, $g_s \to \infty$. The first term on the left-hand side of Eq. (6) is the surface sensible heat flux (H), the second term is the surface latent heat flux (λE), and the right-hand side is the surface net radiation flux (R_n). The ground heat flux is neglected here, since it is typically relatively small over long time scales.

f. *Near-surface relative humidity*

Unlike Robinson and Catling (2012), our theory includes a hydrologic cycle. To solve for evapotranspiration and precipitation requires an equation for near-surface RH. We use a simple theory derived for RH over land in a previous study (McColl and Tang 2024):

$$\mathrm{RH} = \exp[-(1 - \mathrm{EF})], \quad (7)$$

where EF is the ratio of the surface latent heat flux to the sum of surface sensible and latent heat fluxes. The equation is conceptually similar to the energy balance of the atmosphere between the surface and the LCL in RCE, in which the surface sensible heat flux is balanced by diabatic cooling from radiative flux divergence and the reevaporation of falling hydrometeors. It has been shown to be quantitatively accurate in the annual and zonal mean over land, through comparison with both reanalysis data and cloud-permitting RCE simulations. While it somewhat overstates RH under extremely dry conditions, a more complicated version fixes that problem [Eq. (B2) in McColl and Tang 2024]. Here, we choose to use Eq. (7) because it is simpler and is sufficiently accurate for our purposes. Further details on the derivation, validation, and implications of this equation can be found in McColl and Tang (2024).

g. *Limitations*

Our theory is subject to important limitations. Like the most similar prior theory (Robinson and Catling 2012), it approximates longwave radiative transfer as gray. This is a major simplification, and gray gas radiative transfer has well-known limitations in particular circumstances (Pierrehumbert 2010; Jeevanjee and Fueglistaler 2020a,b). It also does not explicitly model shortwave radiative transfer, although it does permit tropospheric shortwave absorption [when $F_*^{\mathrm{net}}(\tau_0) < F_*^{\mathrm{net}}(\tau_c)$]. Shortwave radiative absorption becomes very important in some circumstances, particularly in hothouse climates (Jeevanjee and Romps 2018; Seeley and Wordsworth 2021; Liu et al. 2024) or in the presence of significant aerosol perturbations (Dagan and Eytan 2024). We further discuss limiting cases for which the gray radiative transfer scheme makes the theory inapplicable in section 4 and the appendix. In addition, the optical depth τ_0 is treated as a fixed, external parameter, even though it is, in part, a function of atmospheric water vapor. In fact, we might expect it to be greater in wetter climates. Prior studies have made similar approximations (e.g., O'Gorman and Schneider 2008). When varying τ_0, our results should be interpreted as responses to changes in total longwave absorption, rather than any specific greenhouse gas. However, our cloud-permitting simulations do not use gray radiative transfer schemes and include radiatively interactive water vapor. Despite these limitations, our theory is able to reproduce some of the most important features of those simulations (section 3).

Another limitation is that our theory does not internally determine the lapse rate but requires its specification as a parameter. The theory cannot be used to understand climate sensitivity, since the lapse rate feedback, and thus the lapse rate itself, plays an important role in determining climate sensitivity. However, other aspects of climate are less sensitive to the lapse rate, including much of the hydrologic cycle (Takahashi 2009), which is the focus of our study.

Our study treats RCE as an analog for inland continental regions that extend into midlatitudes. More broadly, it assumes there are no lateral atmospheric fluxes. Since lateral atmospheric fluxes are clearly not zero over land, how justified is this analogy? In this study, the flux divergences of vertically integrated specific humidity (q), dry static energy (d), and moist static energy ($m = d + \lambda q$) are all zero, on average. However, given the presence of observation errors, and interest in this case as an approximate analogy, many studies accept a range of flux divergence values (including zero) in their definition of RCE. There are at least three ways to choose that range. First, the range can be set to a symmetric interval around zero with fixed end points. For example, Jakob et al. (2019) used observations to estimate the dry static energy flux divergence [div(d)] at different spatial and temporal scales, where they defined regions with $|\mathrm{div}(d)| \leq 50$ W m^{-2} as in RCE. As they note, any nonzero value within this range could be reasonably attributed to observation error and is effectively indistinguishable from zero. While their study focuses on various regions in the tropical Pacific that are *not* in RCE, even in the annual mean, their results show that many regions over land appear to be in RCE, according to their definition (see their Fig. 2a). Similar results are shown in Fig. 1 of Dagan and Stier (2020), who also examine div(d) and the specific humidity flux divergence [div(q) = $P - E$ at equilibrium]. Second, the range can be set to a symmetric interval around zero with spatially varying end points, e.g., with end points set to be a fixed

fraction of a flux. This approach accounts for the fact that fluxes in the budgets for m, d, and q are typically smaller over land at higher latitudes, which suggests that the threshold of 50 W m^{-2} should also be smaller in these regions. Dagan and Stier (2020) show, in their Fig. S2, that $|\mathrm{div}(q)|/P$ is often considerably smaller over land than ocean, with a typical value of ~20% (with some spread in both directions). Estimated values of $|\mathrm{div}(d)|/P$ are considerably larger, however. Third, the range can be set to an asymmetric interval around zero with spatially varying end points. Miyawaki et al. (2022) adopt this approach, classifying regions as in RCE at steady state when $\mathrm{div}(m)/Q_R < 0.1$, where Q_R is the radiative heating rate of the column. Since Q_R is typically negative, regions of strong m flux divergence are included in this definition. They justify this choice with the argument that "temperature profiles in regions of divergence are set by convective adjustment." Based on this definition, they find that RCE is prominent over land in the zonal and annual mean, as far as 40°N. Overall, the available evidence suggests RCE is a useful analog of inland continental climate, outside high latitudes, while also recognizing that there are significant deviations from this idealized model in the real world.

Our study focuses on radiative–convective equilibria but does not say anything about transient dynamics, including those related to soil moisture memory (Delworth and Manabe 1989; McColl et al. 2017, 2019a; Rahmati et al. 2024) and soil moisture–precipitation feedbacks (e.g., Hohenegger and Stevens 2018). It also does not address potential sensitivity to initial conditions. In RCE over a saturated surface with fixed surface temperatures, the final equilibrium state is insensitive to initial conditions. However, if the surface temperature is not fixed (as in our study), some evidence suggests that the final equilibrium state can be sensitive to initial conditions, implying the existence of multiple equilibria (Renno 1997). Rochetin et al. (2014) found multiple equilibria when simulating RCE over a land surface with interactive soil moisture. They found that clouds played an important role in the development of multiple equilibria, although their model did not resolve convection. Abbott and Cronin (2023) found multiple equilibria in cloud-permitting simulations of an idealized land surface with interactive soil moisture. However, those simulations used the weak temperature gradient approximation, rather than RCE. All of this suggests that multiple equilibria may well exist in RCE over land, but they are not seen in our simulations, where surface temperature evolves freely. In any case, our theory can be understood as providing insight into *one* equilibrium state, without necessarily implying that it is *the only possible* equilibrium state.

3. Evaluating the theory with cloud-permitting simulations

We conducted cloud-permitting simulations over an idealized land surface in RCE using the System for Atmospheric Modeling (SAM; Khairoutdinov and Randall 2003), version 6.11.1. The model environment is the same as in McColl and Tang (2024), with a homogeneous grassland surface simulated by the Simplified Land Model (SLM; Lee and Khairoutdinov 2015). We use the Community Atmosphere Model, version 3 (CAM3), radiative transfer scheme, a single-moment microphysics scheme, and a 1.5-order turbulent kinetic energy (TKE) subgridscale turbulence closure scheme.

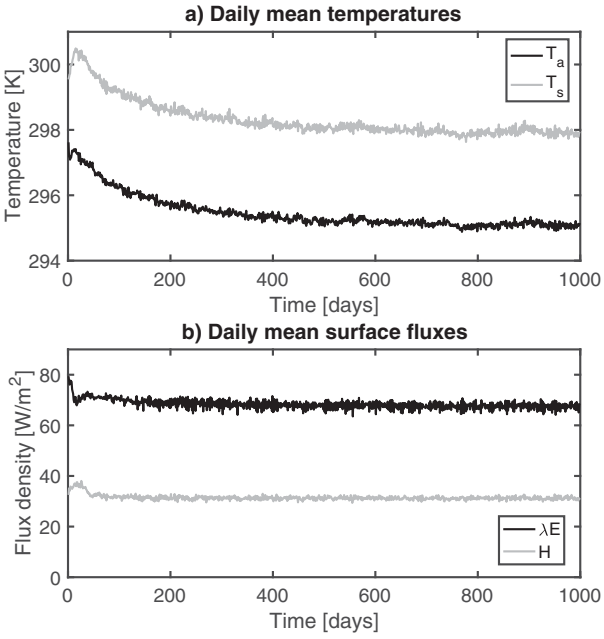

FIG. 2. Example simulated time series of daily mean (a) surface (T_s) and near-surface air (T_a) temperatures and (b) latent (λE) and sensible (H) heat fluxes from one simulation (latitude 12°N and soil saturation $s = 0.4$).

Nine simulations were conducted, using three different values for solar forcing (equivalent to solar forcing at latitudes of 8°, 12°, and 16°N) and three different values of soil saturation (the ratio of the volumetric soil moisture to the soil porosity $s = 0.2$, 0.4, and 0.6). The domain size is 192 km × 192 km, with a horizontal spatial resolution of 3 km and doubly periodic lateral boundary conditions. Unlike typical RCE simulations over an ocean surface (Wing et al. 2018), we included a diurnal cycle in our solar forcing. We did not include a seasonal cycle: Instead, we repeated the solar forcing for 1 January for 1000 days to reach a radiative–convective quasi-equilibrium state (Fig. 2), with the last 30 days of the simulation used in our analysis. For simulations at latitudes 8°, 12°, and 16°N, the average insolation at the TOA is 372, 349, and 324 W m^{-2}, respectively; the average net shortwave radiation at the TOA is 274, 251, and 229 W m^{-2}, respectively; and the average net shortwave radiation at the surface is 177, 172, and 161 W m^{-2}, respectively. The surface albedo is approximately 0.1 in all simulations.

Our wettest simulations ($s = 0.6$) approximately correspond to a saturated soil at field capacity. More specifically, if we define the "field capacity" s_{fc} as corresponding to a soil saturation value for which the hydraulic conductivity is 0.1 mm day^{-1}, then

$$s_{\mathrm{fc}} = \frac{\theta_{\mathrm{fc}}}{\theta_s} = \left(\frac{0.1}{K_s}\right)^{1/(2b+3)} = 0.62.$$

Here, we have used the standard Brooks–Corey formulation relating hydraulic conductivity to soil saturation, θ_{fc} and θ_s are the volumetric field capacity and porosity, respectively, K_s is

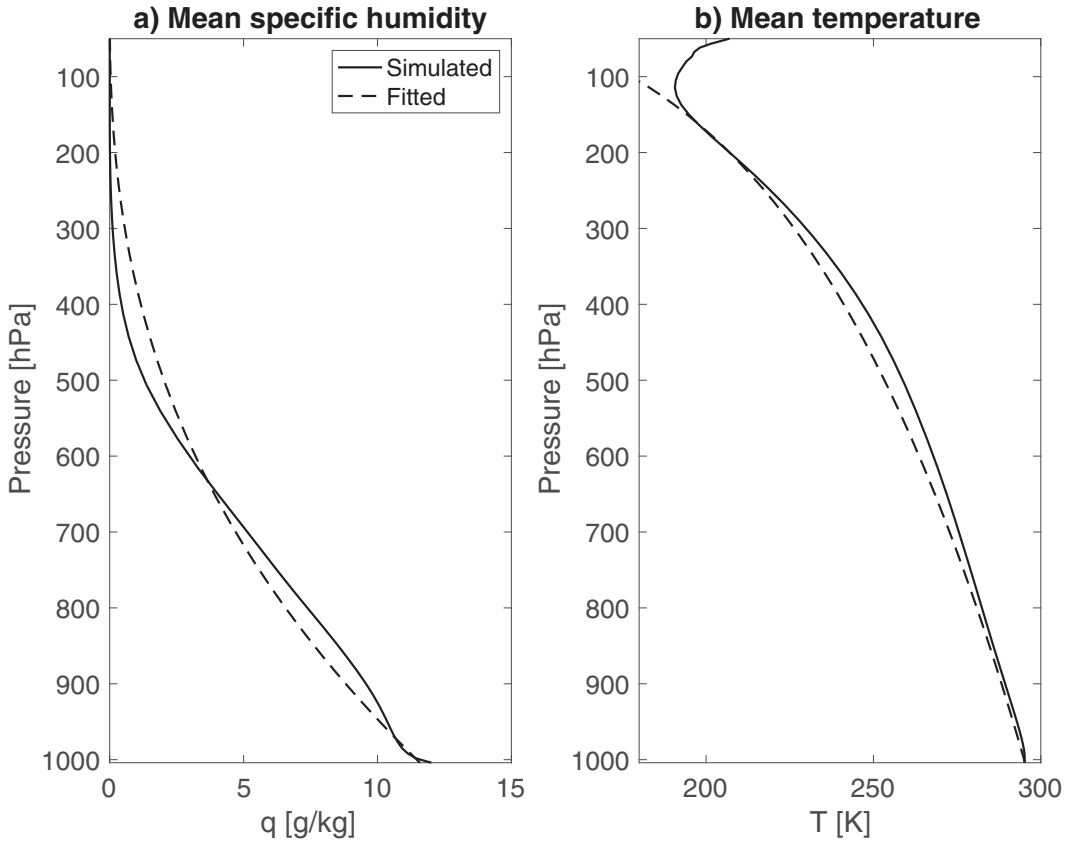

FIG. 3. Example simulated vertical atmospheric profiles of mean (a) specific humidity and (b) temperature from one simulation (latitude 12°N and soil saturation $s = 0.4$). The simulated profiles (solid lines) are compared with the corresponding approximations used in the theory, fitted to the simulated profiles (dashed lines): Eq. (8) for specific humidity and Eq. (2) for temperature.

the saturated hydraulic conductivity (328 mm d^{-1} in our simulations, a function of soil texture), and $b = 6.89$ is the Brooks–Corey parameter (a function of soil texture). This scheme is used in our simulations, with a soil comprising 40% sand and 25% clay. Qualitatively, this means s_{fc} is an approximate upper bound on soil saturation in our simulations over sufficiently long time scales. To fix soil moisture, we relaxed soil saturation s to 0.2, 0.4, and 0.6 over a time scale of 24 h. This scheme couples soil moisture to the atmosphere on short time scales (subdaily), while enforcing a prescribed soil moisture value on longer time scales. As a result, the equilibrium soil saturation differs somewhat from these three assigned values. Specifically, the average soil saturation at equilibrium is 0.29 for "$s = 0.2$," 0.47 for "$s = 0.4$," and 0.58 for "$s = 0.6$."

To compare our theory with the simulations, we first estimated several of the theory's parameters and inputs from the simulations. The longwave broadband emissivity at the surface (ϵ_s) is assumed equal to 0.95, a value similar to that used in the simulations. The time-averaged aerodynamic conductance (g_a) and surface conductance for water vapor (g_s) were estimated for each simulation by inverting the equations for H and λE in Eq. (6). The lapse rate parameter (β) was estimated by fitting Eq. (2) to simulated time-averaged vertical temperature profiles (as in Fig. 3b). Following Beucler and Cronin (2016), we treated water vapor as the dominant longwave absorber and thus estimated n by fitting the relation

$$q(p) = q_0\left(\frac{p}{p_0}\right)^n \tag{8}$$

to time-averaged vertical specific humidity profiles (as in Fig. 3a). For all simulations, τ_c was set to a fixed value of 0.01. We tested various reasonable values of τ_c, corresponding to tropopause pressure levels between 100 and 300 hPa, and found our results were not particularly sensitive to the choice of τ_c (not shown). Similarly, for all simulations, F_c^- was set at a fixed value of 9.3 W m^{-2}, corresponding to the average value across all simulations. Our results are also not particularly sensitive to varying F_c^- within the range observed in our simulations (not shown). We directly used the time-averaged net shortwave radiation at the surface ($F_*^{\mathrm{net}}(\tau_0)$) from each simulation. For net shortwave radiation at the tropopause ($F_*^{\mathrm{net}}(\tau_c)$), we estimated it as a weighted average of equivalent values at the top of the atmosphere and at the surface: $F_*^{\mathrm{net}}(\tau_c) = 0.93F_*^{\mathrm{net}}(0) + 0.07F_*^{\mathrm{net}}(\tau_0)$. This weighting was estimated by averaging across all simulations. Our results are not especially sensitive to this weighting. In section 4, we further simplify by neglecting shortwave absorption entirely. Finally, we estimated τ_0 for each simulation from the tropopause energy balance [Eq. (5)].

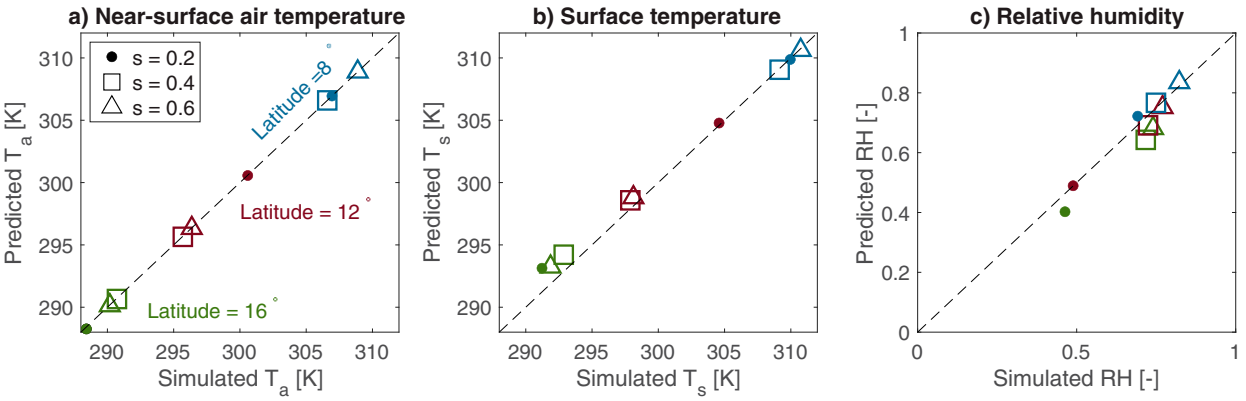

FIG. 4. Evaluating the theory with cloud-permitting numerical simulations. (a) Comparison between simulated near-surface air temperature (T_a) and the predicted value from the simple theory. Each dot corresponds to one numerical simulation, with the fixed soil moisture value for the simulation denoted by the marker type (see legend), and the latitude denoted by the marker color. The dashed line is the one-to-one line. (b) As in (a), but for surface temperature (T_s). (c) As in (a), but for near-surface RH.

In summary, we estimate or prescribe values for 10 parameters [ϵ_s, τ_0, τ_c, β, n, g_a, g_s, F_c^-, $F_*^{\text{net}}(\tau_c)$, and $F_*^{\text{net}}(\tau_0)$]. The theory's three governing equations [Eqs. (5)–(7)] are then solved for three unknowns (T_a, T_s, and RH). A simpler version of this theory will be considered in section 4.

Comparisons between simulated and theory-predicted surface temperature (T_s), near-surface air temperature (T_a), and near-surface RH are shown in Figs. 4a–c. The theory performs reasonably well for all three variables. Errors in the theory's predictions are further reduced if parameters or inputs that were prescribed the same value across all simulations (ϵ_s, τ_c, F_c^-) are tuned to case-specific values (not shown). The predicted fluxes correlate reasonably well with the simulated values, although they become increasingly biased at higher latitudes (not shown). While several parameters have been tuned to fit the simulations, it was not obvious a priori that our simple theory would be capable of matching the simulations this well.

Perhaps surprisingly, both surface and near-surface air temperatures do not monotonically decrease with increasing soil moisture (Figs. 4a,b). We will show shortly that the dominant controls on surface and near-surface air temperature in our simulations are β/n and $F_*^{\text{net}}(\tau_c)$, rather than soil moisture or related quantities.

Next, we conduct sensitivity tests to understand which parameters are most important. First, we consider an essentially saturated surface ($s = 0.6$; Fig. 5). The tropopause energy balance [Eq. (5)] primarily determines T_a and, by extension, T_s. As an illustration of this point, in Figs. 5a and 5b, we set the surface conductance used in the theory's predictions to a large value consistent with a saturated surface and compare it to cloud-permitting simulations with the largest surface conductance values (corresponding to cases with $s = 0.6$) at each latitude. Other parameters are assigned their average values across all simulations, except for $F_*^{\text{net}}(\tau_c)$ and β/n, which are assigned their simulation-specific estimated values. The theory provides reasonable estimates of surface and near-surface air temperature. Both surface and near-surface air temperatures increase with increasing β/n and $F_*^{\text{net}}(\tau_c)$. This result can be understood by referring to Eq. (5). In Eq. (5), when τ_0 is sufficiently large, the first term on the right-hand side becomes small. The third term on the right-hand side, F_c^-, is also typically an order of magnitude smaller than the other terms. Since τ_0 only varies a little between simulations, Eq. (5) implies that $F_*^{\text{net}}(\tau_c)$ and β/n should be the main sources of variability, as found here.

In contrast to air and surface temperatures, for the saturated surface considered here, RH (Fig. 5c), H (Fig. 5d), and λE (Fig. 5e) do not vary much in response to changes in $F_*^{\text{net}}(\tau_c)$ and β/n. These quantities are primarily sensitive to surface saturation (g_s). The theory's sensitivity to g_s and τ_0 is shown in Fig. 6, where all other parameters are set to their average values at 12°N. The three superimposed data points indicate the three cloud-permitting simulations at 12°N, which broadly correspond to the theory's predictions. Similar results are obtained when fixing parameters to their average values at 8° and 16°N (not shown). These results can be understood as follows. Higher soil moisture (and thus higher g_s) causes a higher evaporative fraction, which increases λE (Fig. 6e) at the expense of H (Fig. 6d). Since relative humidity scales with the evaporative fraction [Eq. (7)], it is higher over soils with higher g_s (Fig. 6c), all else equal. Surface temperature slightly declines in response to increasing g_s, but the effect is small (Fig. 6a). Perhaps surprisingly, when τ_0 is small, increasing g_s leads to (small) increases in T_a (Fig. 6b). In this case (small τ_0), surface longwave emission is an important contributor to the tropopause energy balance [Eq. (5)]. Since increasing g_s cools the surface and, therefore, reduces surface longwave emission, Eq. (5) requires that near-surface air temperatures must rise to compensate. However, the overall magnitude of this response is small. To better understand these results, we turn to a simpler version of the theory in the next section.

4. Special cases and analytic solutions

To build intuition, in this section, we consider several special cases of the theory proposed in the previous section. For maximum simplicity, we consider the case of an all-troposphere

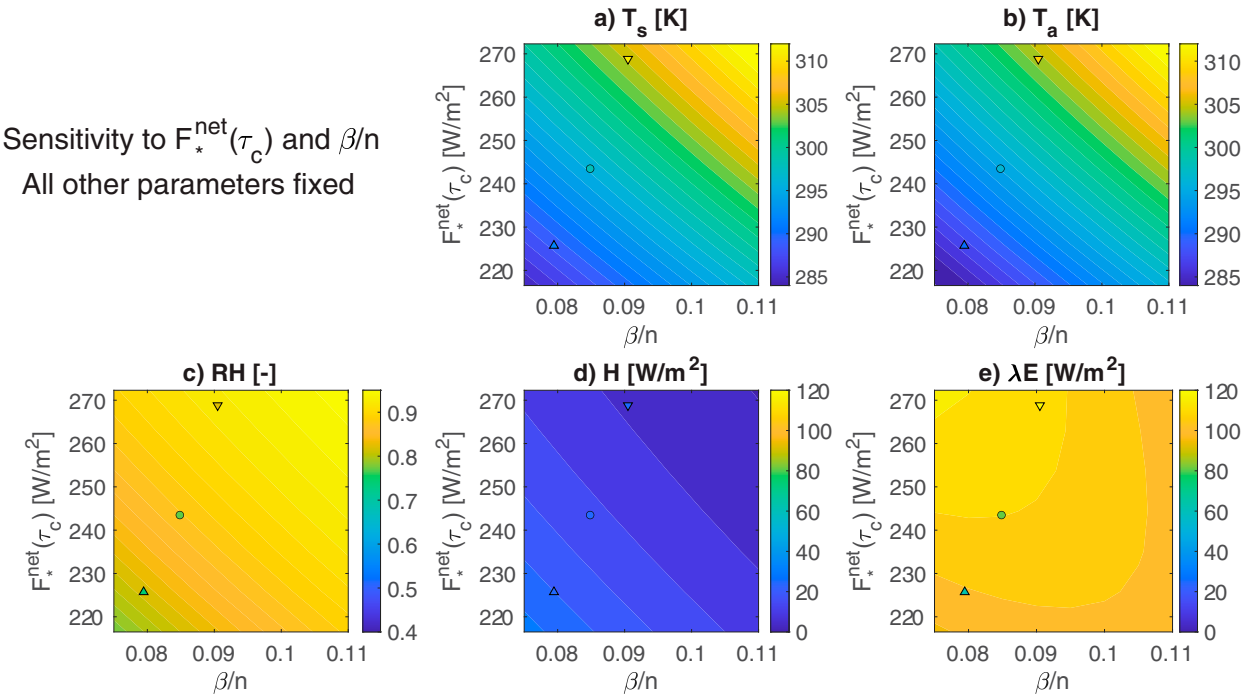

FIG. 5. Sensitivity of the theory to varying $F_*^{\mathrm{net}}(\tau_c)$ and β/n, for a saturated surface. Results are shown for (a) T_s, (b) T_a, (c) RH, (d) H, and (e) λE. For other parameters, the following values are used: $g_s = 10^6$ m s^{-1}, $g_a = 0.0115$ m s^{-1}, $\tau_0 = 2.1$, $F_*^{\mathrm{net}}(\tau_0) = 170$ W m^{-2}, and $n = 2$. The three points marked on each panel correspond to the three cloud-permitting simulations with the wettest soil ($s = 0.6$)—at 8°N (downward triangles), 12°N (circles), and 16°N (upward triangles). The marker color corresponds to the actual value for that simulation.

atmosphere ($\tau_c = F_c^- = 0$) that is completely transparent to shortwave radiation [$F_*^{\mathrm{net}}(\tau_0) = F_*^{\mathrm{net}}(\tau_c)$]. In addition, we approximate ϵ_s as 1. For notational simplicity, we set $D = 1$, which can be thought of as absorbing the diffusivity factor into the definition of τ (Pierrehumbert 2010).

Then, Eqs. (5) and (6) can be rewritten as

$$\begin{aligned} F_*^{\mathrm{net}}(\tau_0) &= \sigma T_s^4 e^{-\tau_0} + \sigma T_a^4 \int_0^{\tau_0} \left(\frac{\tau'}{\tau_0}\right)^{(4\beta)/n} e^{-\tau'} d\tau' \\ &= \sigma T_s^4 e^{-\tau_0} + \sigma T_a^4 \tau_0^{-(4\beta)/n} \left(\Gamma\left[1 + \frac{4\beta}{n}\right] - \Gamma\left[1 + \frac{4\beta}{n}, \tau_0\right]\right), \end{aligned} \tag{9}$$

$$\begin{aligned} &\rho c_p g_a (T_s - T_a) + \rho\lambda \frac{g_s g_a}{g_s + g_a} [q^*(T_s) - \mathrm{RH} q^*(T_a)] \\ &\quad = F_*^{\mathrm{net}}(\tau_0) - \sigma T_s^4 + \sigma T_a^4 \int_0^{\tau_0} \left(\frac{\tau'}{\tau_0}\right)^{(4\beta)/n} e^{-(\tau_0 - \tau')} d\tau' \\ &\quad = F_*^{\mathrm{net}}(\tau_0) - \sigma T_s^4 + \sigma T_a^4 e^{-\tau_0} (-\tau_0)^{-(4\beta)/n} \\ &\qquad \times \left(\Gamma\left[1 + \frac{4\beta}{n}, -\tau_0\right] - \Gamma\left[1 + \frac{4\beta}{n}\right]\right), \end{aligned} \tag{10}$$

where $\Gamma(a, x) = \int_x^\infty t^{a-1} e^{-t} dt$ is the upper incomplete gamma function, and the standard gamma function is $\Gamma(a) \equiv \Gamma(a, 0)$. Both Robinson and Catling (2012) and Pierrehumbert (2010) derive analytic solutions invoking gamma functions for similar problems. The cases they consider typically use fixed (rather than interactive) surface temperatures and saturated (rather than water-limited) surfaces. Pierrehumbert (2010) considers water-limited, unsaturated surfaces in a few idealized cases in his Chapter 6 but does not incorporate an interactive equation for RH, as we do here [Eq. (7)]. As we will show, the interactive RH response to water limitation is highly consequential.

Next, we consider several limiting cases. For completeness, in the appendix, we consider three cases in which our theory fails ($\tau_0 \to \infty$, $\tau_0 \to 0$, and $g_a = 0$), all of which correspond to climates that are radically different from that of the modern Earth. Our theory is accurate in a fourth limit ($g_a \to \infty$) that bears some useful resemblance to the modern Earth. We will provide analytic solutions for this case. In section 5, we consider two further limiting cases ($g_s \to \infty$ and $g_s = 0$) in the context of hydrological sensitivity.

Strongly mixed limit: $g_a \to \infty$

In this section, we consider a limiting case that bears some useful resemblance to the modern Earth and permits analytic solutions: the strongly mixed limit, in which $g_a \to \infty$. The aerodynamic conductance increases with increasing surface winds, surface roughness, or surface heating. All of these changes promote greater turbulent mixing. In the strongly mixed limit, the surface temperature and the near-surface air temperature must converge ($T_s \to T_a$), to ensure the surface sensible heat flux does not diverge to infinity and violate the surface energy balance. Replacing surface temperature with near-surface air temperature in Eq. (9) results in the relation:

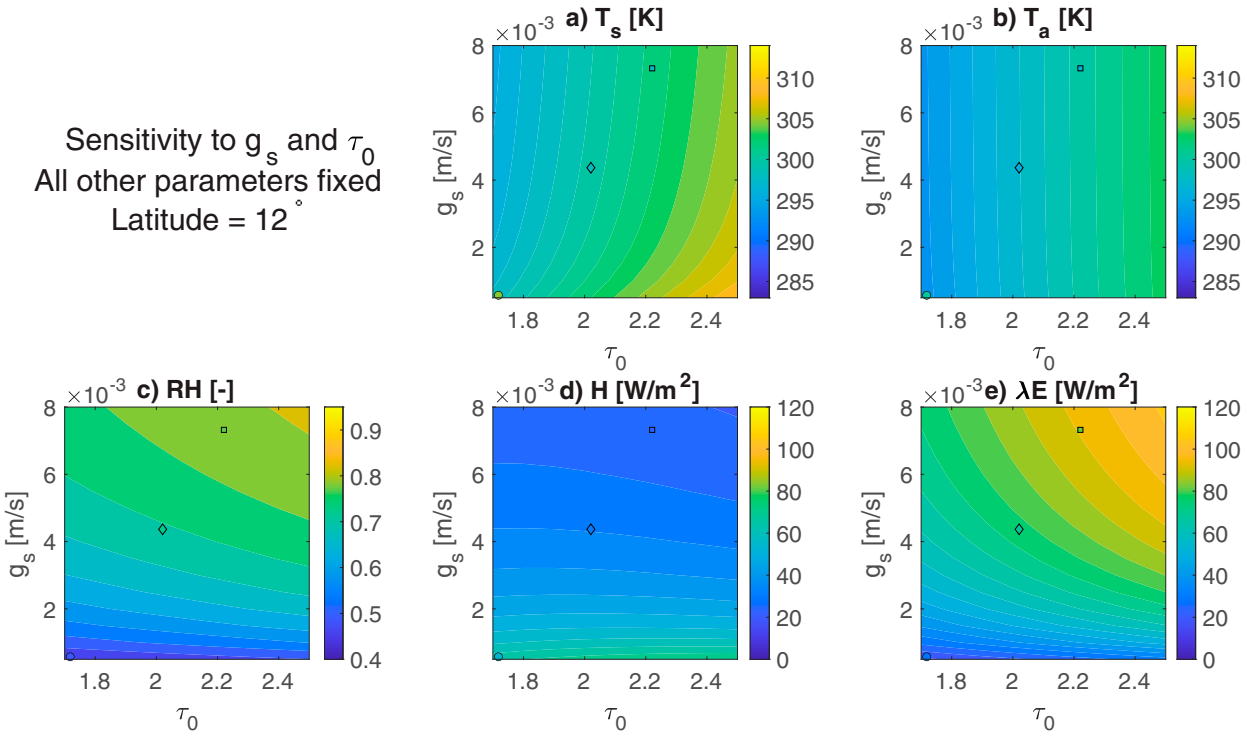

FIG. 6. Sensitivity of the theory to varying g_s and τ_0 at 12°N. Results are shown for (a) T_s, (b) T_a, (c) RH, (d) H, and (e) λE. Here, g_a is assigned the same value as in Fig. 5. Since shortwave radiation and atmospheric profiles largely control temperature (Fig. 5), we use the average values of shortwave radiation [$F_*^{\mathrm{net}}(\tau_c)$ and $F_*^{\mathrm{net}}(\tau_0)$] and β/n at 12°N. Corresponding results for 8° and 16°N are qualitatively similar (not shown). The three points marked on each panel correspond to three cloud-permitting simulations, with circles, diamonds, and squares corresponding to increasing soil saturation s. The marker color corresponds to the actual value for that simulation.

$$T_a = T_s = \left\{ \frac{F_*^{\mathrm{net}}(\tau_0)}{\sigma\left[e^{-\tau_0} + \tau_0^{-(4\beta)/n}\left(\Gamma\left[1+\frac{4\beta}{n}\right] - \Gamma\left[1+\frac{4\beta}{n}, \tau_0\right]\right)\right]} \right\}^{1/4}, \tag{11}$$

where we have chosen the only real and positive solution to the quartic equation. Replacing surface temperature with near-surface air temperature in the right-hand side of Eq. (10) (which equals the surface net radiation R_n) and substituting in Eq. (11) results in

$$R_n = F_*^{\mathrm{net}}(\tau_0) \times \left[1 - \frac{1 + e^{-\tau_0}(-\tau_0)^{-(4\beta)/n}\left(\Gamma\left[1+\frac{4\beta}{n}\right] - \Gamma\left[1+\frac{4\beta}{n}, -\tau_0\right]\right)}{e^{-\tau_0} + \tau_0^{-(4\beta)/n}\left(\Gamma\left[1+\frac{4\beta}{n}\right] - \Gamma\left[1+\frac{4\beta}{n}, \tau_0\right]\right)}\right]. \tag{12}$$

The strongly mixed limit will prove useful for understanding some aspects of our simulations (for which the aerodynamic conductance is finite). In Eq. (11), the surface temperature is entirely determined by $F_*^{\mathrm{net}}(\tau_0)$, β/n, and τ_0. This is qualitatively consistent with our simulations, for which $F_*^{\mathrm{net}}(\tau_0)$ and β/n explain most of the variability in T_s and T_a (Fig. 5), whereas g_s explains relatively little (Fig. 6). In our theory, surface water limitation mainly constrains the evaporative fraction and RH, rather than near-surface air temperature. As noted earlier, our theory does not include any interaction between surface water limitation and lapse rate.

Figure 7 shows T_a, $T_s - T_a$, and R_n across a wide range of climates, obtained by varying τ_0. Starting with T_a, the strongly mixed limit provides a reasonably accurate approximation of equivalent values of T_a obtained with finite aerodynamic conductance. In the limit of large τ_0, the surface temperature term in Eq. (9) becomes negligible, and T_a is entirely determined by the tropopause energy budget [Eq. (9)], that implies that T_a is insensitive to surface conductance for sufficiently large τ_0 (note that, while this makes sense for a gray gas atmosphere, it does not account for spectral windows in the real atmosphere). For lower τ_0, T_a is determined jointly by both the tropopause and surface energy balances; thus, T_a is somewhat sensitive to surface conductance.

While these differences are relatively small, it is perhaps surprising that, for a given τ_0 and finite aerodynamic conductance, near-surface air temperatures are (very slightly) lower for drier surfaces, rather than higher (Fig. 7a; note that the differences in temperature are too small to be visible here). In our theory, this is explained by differences in surface temperature T_s. While T_s and T_a are identical in the strongly mixed limit, T_s is greater than T_a when the aerodynamic conductance is finite. The difference is greater for drier surfaces (Fig. 7b), resulting

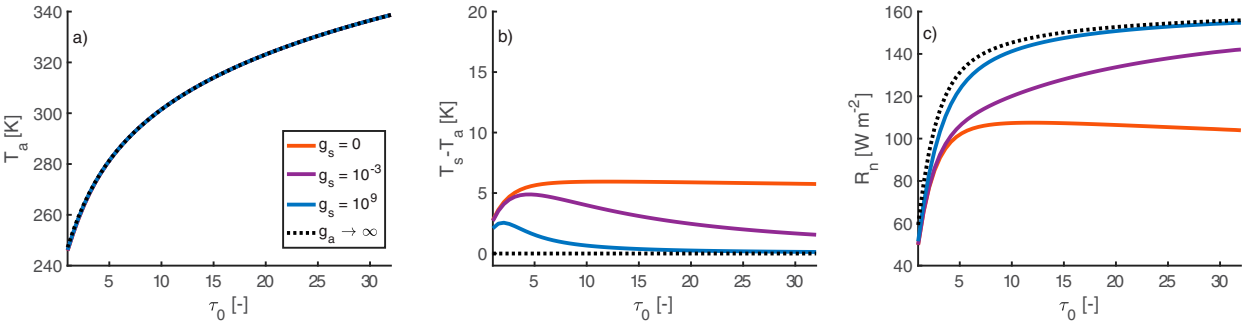

FIG. 7. (a) Sensitivity of near-surface temperature (T_a) to varying τ_0 in the simple model [Eqs. (9) and (10)]. Unless otherwise specified, $g_a = 0.015$ m s^{-1}, $F_*^{\text{net}}(\tau_0) = 165.9$ W m^{-2}, $n = 2$, and $\beta = 0.2$. Three solutions with different values of surface conductance are shown. A fourth solution is shown for the strongly mixed limit [$g_a \to \infty$, Eq. (11)], for which the solutions are insensitive to surface conductance. (b) As in (a), but for $Ts - T_a$. In the strongly mixed limit, $T_s - T_a \to 0$. (c) As in (a), but for R_n. In the strongly mixed limit, R_n is given by Eq. (12).

in a larger radiative loss to space from the surface and slightly lower near-surface air temperatures (Fig. 7a) and surface net radiation (Fig. 7c). Again, this explanation applies to our simple theory, in which β/n is fixed; in the real atmosphere, both of these quantities will respond to varying g_s, to some extent, which will alter this result.

Why does the strongly mixed limit provide a reasonable approximation of some Earth-like conditions? In short, for Earth-like conditions, a low aerodynamic conductance solution is an unstable equilibrium. If the aerodynamic conductance is low, a strongly unstable near-surface temperature gradient arises, which promotes strong convective sensible heat fluxes and associated turbulent mixing, causing the aerodynamic conductance to rise.

The strongly mixed limit also provides a self-consistent way to require the difference between surface temperature and near-surface air temperature to be small. The difference between these quantities is typically small for Earth-like conditions, particularly after averaging in space and time. However, simply setting these quantities equal and using a finite aerodynamic conductance would require the sensible heat flux to be zero. This is a very poor approximation over land. Instead, the strongly mixed limit results in $T_s \to T_a$ without requiring zero sensible heat flux.

In the next section, we consider the limiting cases of a saturated ($g_s \to \infty$) and dry ($g_s \to 0$) surface, in the context of understanding hydrological sensitivity.

5. An analytic theory for hydrological sensitivity

In this section, we use the strongly mixed limit to understand hydrological sensitivity over saturated and unsaturated surfaces in RCE. While "hydrological sensitivity" is often defined as the fractional change in precipitation per degree of surface warming, here we use the term as shorthand for the relation between precipitation and temperature. Since we ignore moisture flux convergence, dynamical contributions to hydrological sensitivity (due to, e.g., changes in circulation) are ignored.

Several questions arise:

- Prior studies of hydrological sensitivity over saturated surfaces typically argue that hydrological sensitivity is largely determined by changes in atmospheric radiative cooling (Mitchell et al. 1987; Allen and Ingram 2002; O'Gorman and Schneider 2008; Takahashi 2009; O'Gorman et al. 2012; Pendergrass and Hartmann 2014; Jeevanjee and Romps 2018). Others use a surface energy budget perspective, in which surface quantities dominate the explanation (Boer 1993; Pierrehumbert 2002; Richter and Xie 2008; Andrews et al. 2009; Lorenz et al. 2010; Kleidon and Renner 2013; Siler et al. 2019; Wang et al. 2021). How should these two perspectives be reconciled? The answer is not entirely clear. For example, hydrological sensitivity over saturated surfaces is dependent on the radiative forcing agent (Andrews et al. 2010; O'Gorman et al. 2012; Kleidon and Renner 2013). Even in simulations with simplistic gray radiative transfer, shortwave forcing results in a concave upward relation between temperature and precipitation, whereas longwave forcing results in a concave downward relation (O'Gorman et al. 2012). This difference appears to be inconsistent with certain surface energy budget perspectives on the problem, which do not distinguish between different radiative forcing agents (Siler et al. 2019).
- Prior work on hydrological sensitivity has been conducted over largely saturated surfaces, presumably because most of Earth's surface is ocean. Yet, much of Earth's surface is unsaturated land, particularly in the Northern Hemisphere. And, there are other planets with active hydrological cycles where most of the surface is land rather than ocean. For example, Titan's surface, which includes lakes, seas, and an active "hydrological" cycle of methane and ethane, is dominated by land (Hörst 2017). What happens when the surface is fixed to lower soil saturation? To our knowledge, no prior work has considered this question.

Before addressing these questions, we show that our theory qualitatively reproduces results from similar prior studies. The most natural comparands are O'Gorman and Schneider (2008) and O'Gorman et al. (2012), who both considered hydrological sensitivity over a saturated surface with an interactive surface temperature. These studies also used gray radiative transfer, and O'Gorman and Schneider (2008) included an explicit RCE case (their Fig. 4). Our theory is considerably simpler than the GCM

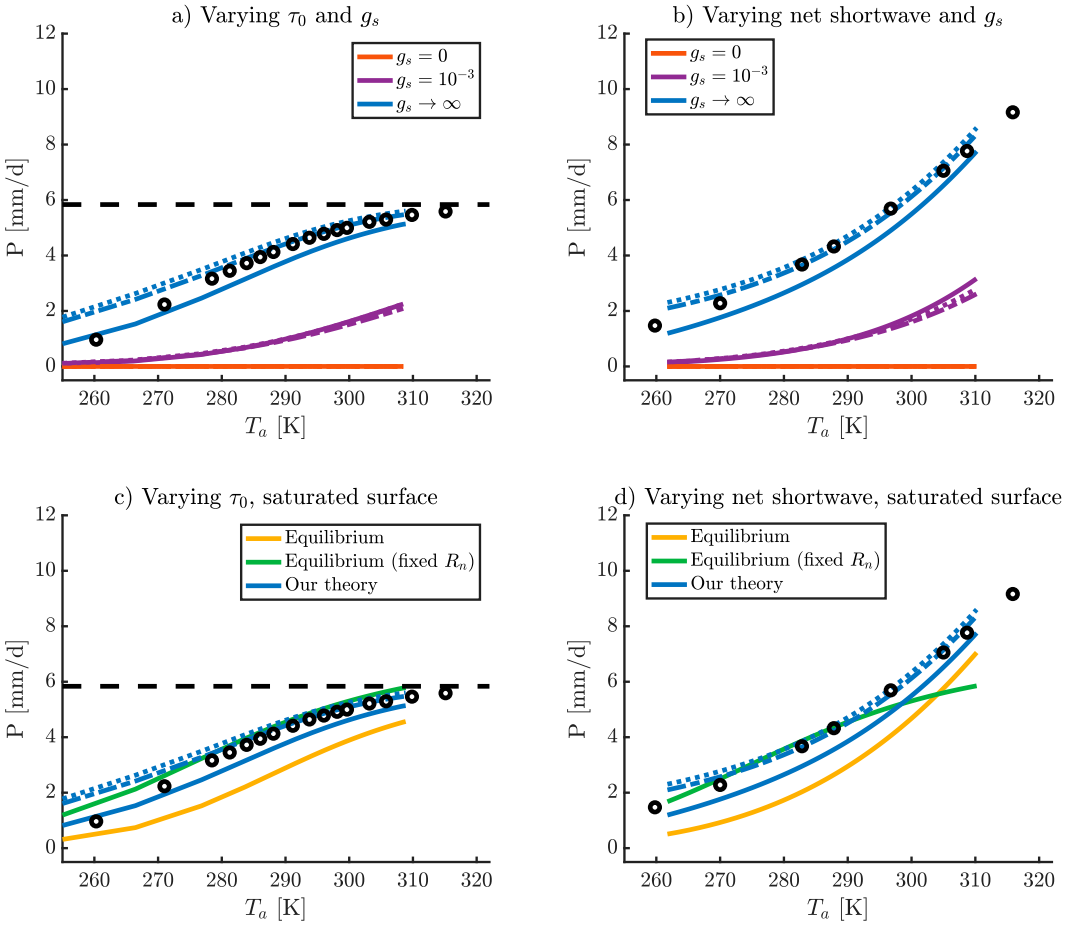

FIG. 8. The relation between precipitation (P) and temperature (T_a) for (a),(c) varying τ_0, (b),(d) net shortwave [$F_*^{\text{net}}(\tau_0)$], and (a),(b) surface conductance (g_s). Solid lines correspond to results with $g_a = 0.015$ m s^{-1}. In (a) and (b), for each surface conductance value, two approximate solutions using the strongly mixed limit [Eq. (16)] are also shown: one using actual values of T_a and R_n [dashed lines, obtained by numerically solving the Eqs. (7), (9), and (10)] and another using Eqs. (11) and (12) to approximate those quantities, respectively (dotted lines). The two approximate solutions for the case with zero surface conductance are not visible because they exactly overlap with the actual solution. Results are compared with those from (a) Fig. 4 of O'Gorman and Schneider (2008) and (b) Fig. 2b of O'Gorman et al. (2012) (black circles). In (a) and (c), the horizontal dashed black line corresponds to a hypothetical case in which all net shortwave radiation is used for evapotranspiration and precipitation. In (c) and (d), two alternative theories that apply to saturated surfaces with the atmosphere fixed at saturation—"equilibrium" evaporation [Eq. (18)] and a variant in which net radiation is held fixed [Eq. (18) but with R_n held fixed, as proposed in Siler et al. (2019)]—are also compared with our theory (with $g_s \to \infty$, representing a saturated surface).

used in these prior studies. To allow a fairer comparison, rather than prescribing the lapse rate by setting β to be a fixed parameter, we assume a moist adiabatic lapse rate that varies with temperature and estimate β using Eq. (9) of Koll et al. (2023). That equation provides an approximate estimate of the bulk lapse rate (β) of a moist adiabat, in terms of the near-surface air temperature. We infer other parameters from the figures and text of O'Gorman and Schneider (2008), where possible; if not, we choose values within a physically reasonable range. The baseline optical depth τ_0 is set at 5.3 and varied linearly between 1 and 60 in Fig. 8a. The baseline net shortwave radiation is set at 165.9 W m^{-2} and varied linearly between 96.2 and 282 W m^{-2} in Fig. 8b. For all simulations, $g_a = 0.015$ m s^{-1} and $n = 2$.

Figure 8 shows the predicted relation between near-surface air temperature and precipitation, obtained by varying τ_0 (Fig. 8a) and net shortwave radiation (Fig. 8b) and for varying levels of surface conductance. Focusing on the saturated case ($g_s \to \infty$), our theory's predictions compare reasonably well to prior studies (black dots), both when varying τ_0 and varying net shortwave radiation. Deviations from the results in O'Gorman and Schneider (2008) likely arise due to a range of differences between the two models. For example, our model neglects Monin–Obukhov stability corrections to the aerodynamic

conductance adopted in O'Gorman and Schneider (2008); the gray radiative transfer schemes are somewhat different; and the model of O'Gorman and Schneider (2008) does not include precipitation reevaporation, which plays an important role in determining the sensitivity of evapotranspiration to relative humidity in our theory (McColl and Tang 2024). Given these myriad differences, the similarity is quite reasonable.

a. Explicit equation for evapotranspiration

Since we neglect moisture flux convergence, in this study, precipitation and evapotranspiration are equivalent. Here, we provide an explicit equation for evapotranspiration that, unlike a common alternative, includes important land–atmosphere feedbacks. We then use this equation later in this section to understand hydrological sensitivity. It is also used in section 6 to understand changes in potential evapotranspiration and aridity with warming.

We start with a standard simplification for the equation for λE [Eq. (6)]. That equation is an implicit equation for evapotranspiration; here, we provide an explicit equation, which will be useful in understanding hydrological sensitivity in the next section. Linearizing $q^*(T_s)$ around T_a, using the definition of H to eliminate $T_s - T_a$, replacing H with $R_n - \lambda E$, and rearranging to solve for λE yields

$$\lambda E = \frac{\overbrace{\frac{\lambda}{c_p}\frac{\lambda q^*(T_a)}{R_v T_a^2}}^{\equiv \epsilon} R_n + \rho \lambda g_a q^*(T_a)(1 - \mathrm{RH})}{\epsilon + 1 + \frac{g_a}{g_s}}, \tag{13}$$

where, as in previous sections, we have neglected the ground heat flux, which is typically small on long time scales over land. Equation (13) is the well-known Penman–Monteith equation (Penman 1948; Monteith 1965); see McColl (2020) for more details on its derivation. It is most accurate when the difference between T_s and T_a is small, as is often the case over land, on average, at least in the current climate. Its main advantage over Eq. (6) is that it is an explicit equation for λE, while Eq. (6) is not.

However, the Penman–Monteith equation does not include an important land–atmosphere feedback, discussed in section 2f: A wet surface, with a high EF, causes high RH. To include this feedback, we approximate Eq. (7) as EF $\approx$ RH, substitute this into Eq. (13), and rearrange to obtain

$$\frac{\lambda E}{R_n} = \frac{\epsilon + \rho \lambda g_a q^*(T_a)/R_n}{\epsilon + \rho \lambda g_a q^*(T_a)/R_n + 1 + \frac{g_a}{g_s}}. \tag{14}$$

This equation relates four nondimensional terms to one another. The first term, $\lambda E/R_n$, is the evaporative fraction. The second term, ϵ, is an increasing function of air temperature. The third term, $\rho \lambda g_a q^*(T_a)/R_n$, is the ratio of two quantities: a hypothetical latent heat flux over a saturated surface in which $T_s = T_a$ and RH = 0, and the surface net radiation. The fourth term, g_a/g_s, is the ratio of the aerodynamic conductance to the surface conductance.

These terms are plotted in Fig. 9 as a function of temperature. Both ϵ and $\rho \lambda g_a q^*(T_a)/R_n$ are strongly increasing functions of temperature. When these terms dominate $1 + g_a/g_s$ (e.g., over wet surfaces and in sufficiently warm climates; Figs. 9a,c), Eq. (14) implies that the evaporative fraction should approach 1 and exhibit little dependence on temperature. This is seen in Fig. 9c where, for sufficiently warm temperatures, the evaporative fraction only increases from 0.7 to 0.9 (an increase of approximately 30%) even as air temperature increases by 35 K. In contrast, when those terms are dominated by $1 + g_a/g_s$ (e.g., over dry surfaces or in sufficiently cold climates; Figs. 9b,d), Eq. (14) implies that the evaporative fraction should exhibit stronger dependence on temperature. This is seen in Fig. 9d where, over the same temperature range, the evaporative fraction increases from approximately 0.1–0.4, an increase of approximately 300%.

Equation (14) has important advantages over the Penman–Monteith equation [Eq. (13)]. Whereas the Penman–Monteith equation requires RH as an exogenous input, our equation does not. Instead, our equation incorporates land–atmosphere feedbacks that require RH to be approximately equal to the evaporative fraction. In the context of our RCE theory, this makes our equation considerably more accurate than the Penman–Monteith equation with RH fixed to a prescribed value, especially over saturated surfaces (Fig. 9c). Of course, to the extent that EF $\neq$ RH, errors will arise, and we expect some calibration of the functional relation between EF and RH will be required if applied to real observations. However, the equation is sufficiently accurate to illustrate our main conceptual points. As we will discuss further in section 6, there is good reason to expect that EF scales with RH even at quite small spatial and temporal scales, based on several lines of evidence.

Note that this equation does not require the assumption of gray radiative transfer, or assume a vertical structure for the water vapor profile, or that the lapse rate is fixed. In the next section, we will consider the strongly mixed limit, which simplifies Eq. (14). When combined with analytic solutions for near-surface air temperature and surface net radiation [Eqs. (11) and (12), which both do require the assumptions listed above], this leads to analytic solutions for hydrological sensitivity in the strongly mixed limit.

b. Hydrological sensitivity in the strongly mixed limit

Next, we return to the strongly mixed limit, which serves as a useful approximation that substantially simplifies the governing equations. In the strongly mixed limit,

$$P = E = \rho g_s q^*(T_a)(1 - \mathrm{RH}). \tag{15}$$

As in the previous section, if we approximate Eq. (7) as EF $= \lambda E/R_n \approx$ RH, substitute this into Eq. (15), and rearrange to solve for P, we obtain

$$P = E = \{(R_n/\lambda)^{-1} + [\rho g_s q^*(T_a)]^{-1}\}^{-1} \equiv \frac{1}{2}\mathcal{H}[R_n/\lambda, \rho g_s q^*(T_a)], \tag{16}$$

where $\mathcal{H}(x, y) = 2(x^{-1} + y^{-1})^{-1}$ is the harmonic mean of x and y. The harmonic mean is heavily weighted toward smaller

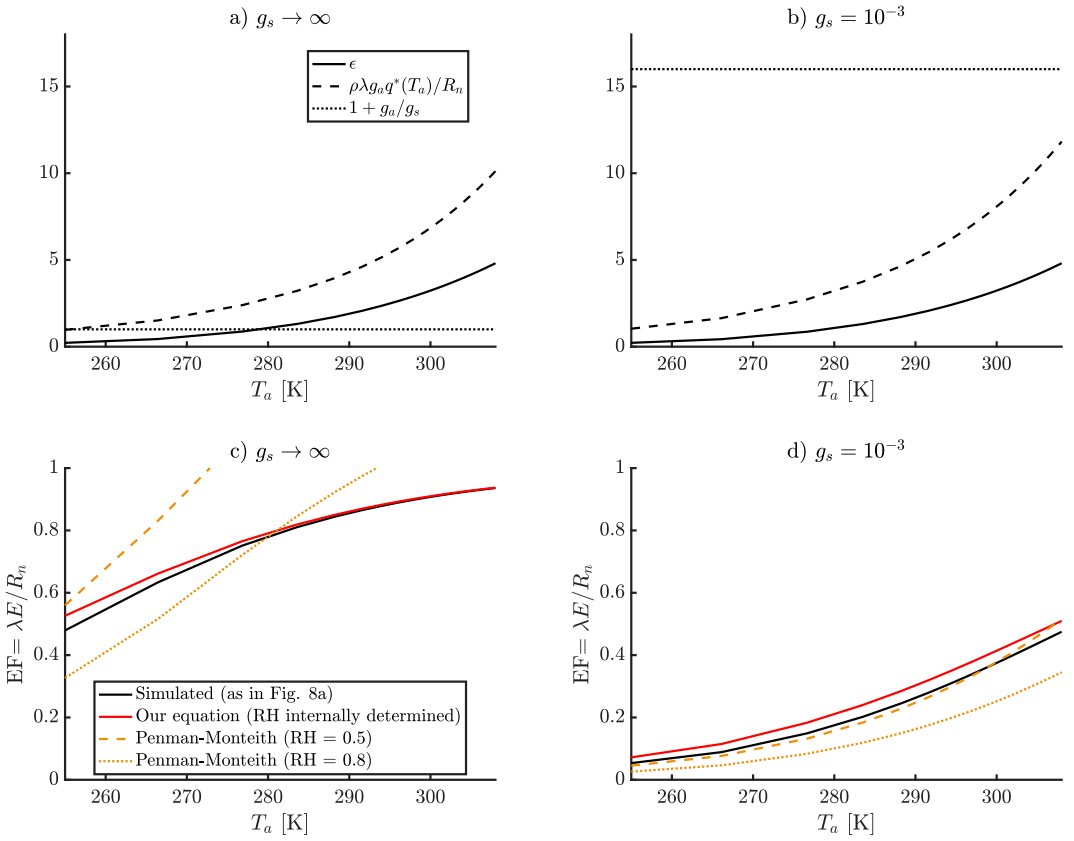

FIG. 9. (a),(b) Terms in the explicit equation for evapotranspiration [Eq. (14)] and their dependence on temperature for (a) a saturated surface ($g_s \to \infty$) and (b) a dry surface ($g_s = 10^{-3}$). Values of T_a and R_n used to estimate terms in all plots are the same as those in Fig. 8a. (c),(d) Comparison of our equation [with RH internally determined, Eq. (14)] to the Penman–Monteith equation [Eq. (13)] with two different fixed values of RH (RH = 0.5 and RH = 0.8) and the true simulated value for (c) a saturated surface and (d) a dry surface. The simulated value is obtained from the same simulations as those used in Fig. 8a.

values: If $x \gg y$ or $y \gg x$, then $(1/2)\mathcal{H}(x, y) \approx \min(x, y)$. More generally, it obeys the following inequality: $(1/2)\min(x, y) \leq (1/2)\mathcal{H}(x, y) \leq \min(x, y)$. We will use these properties in interpreting Eq. (16).

For our purposes, this is a sufficiently reasonable first-order approximation for P, even when the aerodynamic conductance is not infinite. Figure 8 shows this relation, for varying surface conductance. For each surface conductance value, two approximate solutions using the strongly mixed limit [Eq. (16)] are shown: one using values of T_a and R_n determined from the corresponding non–strongly mixed model (dashed lines) and another using analytic solutions for T_a [Eq. (11)] and R_n [Eq. (12)] in the strongly mixed limit (dotted lines). While these approximate solutions somewhat overestimate P for very cold temperatures over saturated surfaces, they are otherwise reasonably accurate given their simplicity.

Two important results follow immediately from Eq. (16):

- Over a sufficiently warm or wet surface [$\rho g_s q^*(T_a) \gg R_n/\lambda$], $P = E \approx R_n/\lambda$. Thus, under these conditions, changes in rainfall with warming follow a *radiative scaling*, determined by changes in surface net radiation (or, equivalently in RCE, changes in atmospheric radiative cooling) with warming. Note that if, instead of invoking the approximation of Eq. (7), we instead assumed constant RH (as in, e.g., Pierrehumbert 2002), we would have $\lambda E \approx \rho\lambda g_s q^*(T_a)(1 - \mathrm{RH})$, which diverges to infinity in the limit of a saturated surface ($g_s \to \infty$). This highlights the importance of near-surface relative humidity in obtaining the correct scaling.
- Over a sufficiently cold and dry surface [$\rho g_s q^*(T_a) \ll R_n/\lambda$], $P = E \approx \rho g_s q^*(T_a)$. Thus, under these conditions, changes in rainfall with warming follow Clausius–Clapeyron scaling.

Since we provide analytic solutions for R_n and T_a in the strongly mixed limit [Eqs. (11) and (12)], the equations provided here for P are also analytic, so long as β is treated as a fixed parameter. Our theory naturally interpolates between the colder, surface-dominated limit and the warmer, atmosphere-dominated limit.

We now use this theory to answer the questions posed earlier. We will use both the strongly mixed limit approximation [Eq. (16)] and the more general relation [Eq. (14)] in the discussion that follows, prioritizing the use of the simpler equation [Eq. (16)] wherever additional complexity is not required.

c. *Reconciling the atmospheric and surface energy budget perspectives*

Our theory quantitatively links the surface and atmospheric energy budget perspectives on hydrological sensitivity. For temperatures typical of current and near-future climates, it predicts that atmospheric radiative cooling (equivalent to R_n in RCE) should be the primary control on precipitation over saturated surfaces (deviations from this scaling at cooler temperatures are discussed further below). While this result is well known based on arguments related to the atmospheric energy budget, our theory derives it using the surface energy budget. The key difference between our theory and that of other surface flux-based arguments (e.g., Siler et al. 2019; Kleidon and Renner 2013) is that our theory directly links RH and the evaporative fraction [Eq. (7); see McColl and Tang (2024) for further details]. Rather than treating RH as an externally specified parameter, it is internally determined by our theory. Takahashi (2009) also solved for RH internally, but that theory is not analytic.

For colder climates unlike those of the modern Earth, precipitation over saturated surfaces deviates from the radiative scaling (O'Gorman and Schneider 2008), indicating that the strongly mixed limit is an overly simplistic approximation. This deviation is second order and not explained by Eq. (16). However, returning to the more general relation [Eq. (14)] and focusing on the saturated limit ($g_s \to \infty$) shows that

$$\begin{aligned} P = E &= \{(R_n/\lambda)^{-1} + [\epsilon R_n/\lambda + \rho g_a q^*(T_a)]^{-1}\}^{-1} \\ &\equiv \frac{1}{2}\mathcal{H}\left[\underbrace{R_n/\lambda}_{\text{Term 1}}, \underbrace{\epsilon R_n/\lambda + \rho g_a q^*(T_a)}_{\text{Term 2}}\right]. \end{aligned} \tag{17}$$

For temperatures typical of current and near-future climates ($T_a \gtrsim 280$ K), ϵ is greater than 1, implying that term 2 is greater than term 1 [since $\rho g_a q^*(T_a) > 0$]. From basic properties of the harmonic mean, this implies that $P \propto R_n/\lambda$ (the radiative scaling), with a constant of proportionality varying between 0.5 and 1 and approaching 1 when term 2 is much greater than term 1. However, for colder climates ($T_a \lesssim 280$ K), ϵ is less than 1, and term 2 need not remain larger than term 1. This implies precipitation over saturated surfaces deviates from the radiative scaling for especially cold temperatures. Under sufficiently cold conditions, it implies that temperature strongly constrains precipitation, consistent with prior studies (Pierrehumbert 2002).

Figures 8c and 8d compare our theory's predictions to alternatives provided in similar prior studies. "Equilibrium evaporation" is the evapotranspiration that would occur over a surface with finite aerodynamic conductance if both the surface and air were saturated ($g_s \to \infty$ and RH = 1, respectively; Slatyer and McIlroy 1961; Priestley and Taylor 1972; Raupach 2000, 2001; McColl 2020). Using Eq. (13), this implies

$$P = E = \frac{\epsilon}{\epsilon + 1}\frac{R_n}{\lambda}, \tag{18}$$

which differs from Eq. (17). Kleidon and Renner (2013) invoked the principle of "maximum power" (related to the principle of "maximum entropy production") to derive an expression for hydrological sensitivity over saturated surfaces that is essentially equivalent to Eq. (18) (although the validity of that principle remains controversial, e.g., Singh and O'Neill 2022). The key difference is that Eq. (18) assumes a saturated atmosphere (RH = 1), whereas our theory [Eq. (17)] does not. Instead, RH is internally determined by our theory. As can be seen in Figs. 8c and 8d, Eq. (18) systematically underestimates precipitation. This is expected since it assumes a saturated atmosphere, whereas the atmosphere is typically subsaturated, which enhances evapotranspiration from a saturated surface. Our theory does not make this assumption and better matches the more complex GCM simulations.

Siler et al. (2019) proposed a simpler variant of equilibrium evapotranspiration, in which surface net radiation is fixed to an arbitrary value in Eq. (18). They used this expression [their Eq. (24)] to argue that changes in precipitation are largely dictated by changes in temperature rather than changes in surface net radiation, even outside of especially cold conditions. This appears to conflict with our result that radiation is the dominant driver of precipitation over saturated surfaces outside of especially cold conditions. However, it is clear from Fig. 8 that the relation between temperature and precipitation is strongly sensitive to the type of radiative forcing applied. If shortwave forcing is increased (Figs. 8b,d), the relation between temperature and precipitation is concave upward, whereas the equation provided by Siler et al. (2019) is incorrectly concave downward (Fig. 8d). If, instead, longwave forcing is increased (by increasing τ_0; Figs. 8a,c), the relation between temperature and precipitation is concave downward, which appears to be in agreement with the equation provided by Siler et al. (2019) (Fig. 8c; note that the absolute values are not meaningful because the net radiation is fixed to an arbitrary value). However, recent work (Liu et al. 2024; Bonan et al. 2024) has shown that precipitation declines with warming in hothouse climates, due to increased atmospheric shortwave absorption by water vapor. This mechanism was not included in any of the idealized GCM simulations shown in Fig. 8 (black circles). This means that, even in the case of increased longwave forcing, the monotonic increasing function of temperature proposed by Siler et al. (2019) will ultimately fail in warmer climates. We conclude that changes in surface net radiation (which is equivalent to atmospheric radiative cooling in RCE) are the more general driver of changes in precipitation, rather than changes in temperature, at least outside especially cold conditions.

d. *Hydrological sensitivity over a fixed dry surface*

How should we expect hydrological sensitivity to differ between a fixed, saturated surface and a fixed, dry surface? Our theory predicts that it should approach a Clausius–Clapeyron scaling under sufficiently dry conditions. A similar, temperature-dependent scaling has been proposed for cold climates (Pierrehumbert 2002), but our theory implies that a similar scaling should also hold for some warm climates, too, so long as the surface is fixed to be sufficiently dry. Figures 8a and 8b show the predicted relation for two fixed, unsaturated surfaces ($g_s = 10^{-3}$ and $g_s = 0$). For a surface fixed to have zero water ($g_s = 0$), there can be no evapotranspiration or precipitation, as predicted by the theory. For a surface fixed

to have a small but nonzero amount of water ($g_s = 10^{-3}$), the relation between temperature and precipitation is concave upward, like the Clausius–Clapeyron relation, and in contrast to the concave downward relation predicted for the fixed, saturated surface ($g_s \to \infty$). Over fixed, dry surfaces, the relation between temperature and precipitation is also qualitatively insensitive to radiative forcing agents (comparing Fig. 8a and Fig. 8b), in contrast to fixed, saturated surfaces.

In climate models, hydrological sensitivity (defined as fractional changes in precipitation per degree of warming) is typically lower over land than ocean (Samset et al. 2018; Allan et al. 2020). Our theory predicts that the relation between temperature and precipitation shifts from concave downward to concave upward for drier surfaces, implying greater fractional changes in precipitation per degree of warming over drier surfaces. However, there is no contradiction with prior literature because we fix surface water limitation (g_s), whereas climate models do not. For example, the plant physiological response to increasing carbon dioxide (CO_2) causes declines in g_s in climate models (Field et al. 1995), which will cause declines in hydrological sensitivity. Those changes are not incorporated here. In addition, changes in moisture flux convergence are entirely neglected here.

Prior theory for hydrological sensitivity has primarily focused on saturated surfaces. Our theory naturally extends recent work. Jeevanjee and Romps (2018) proposed that mean precipitation is primarily dictated by the depth of the free troposphere in temperature coordinates. They showed that this implies that the hydrological sensitivity over a saturated surface approximately scales with $1/(T_s - T_{tp})$, where T_{tp} is the temperature of the tropopause [see Eq. (10) in Jeevanjee and Romps 2018] and T_s is the temperature of the saturated surface. Since the tropopause temperature is approximately fixed across a wide range of surface conditions (Hartmann and Larson 2002; Seeley et al. 2019), it is primarily sensitive to surface temperature. In deriving this back-of-the-envelope approximation, Jeevanjee and Romps (2018) approximated the temperature at the lifting condensation level (T_{LCL}) as equal to T_s. In our theory, drying the surface reduces the near-surface relative humidity, which increases the height of the LCL, and the difference between T_{LCL} and T_s. Therefore, we do not equate these two quantities, resulting in a scaling for hydrological sensitivity of $1/(T_{LCL} - T_{tp})$. Over a dry land surface, the LCL is higher and T_{LCL} is lower, all else being equal, which implies a greater hydrological sensitivity. Our theory is, therefore, consistent with the argument that mean precipitation is primarily determined by the depth of the "free troposphere" (if one defines the "free troposphere" as the troposphere above the LCL). Drying the surface reduces the depth of the "free troposphere" by decreasing near-surface relative humidity and increasing the height of the LCL.

6. Implications for changes in aridity with warming

Our theory also provides important insight into how aridity (typically defined as the ratio PET/P, which is often referred to as the aridity index) should be expected to change with warming.

We begin by reviewing the debate on changes in aridity with warming. A common view is that aridity should increase rapidly with warming, on average. Sherwood and Fu (2014) provided a mechanistic argument for this claim: 1) increases in PET scale with increases in vapor pressure deficit [VPD = $q^*(T_a)(1 - \mathrm{RH})$]; 2) VPD increases with warming faster than precipitation; and 3) therefore, aridity (the ratio PET/P) should rise with warming. Other studies have questioned these claims (Roderick et al. 2015; Milly and Dunne 2016; Swann et al. 2016; Milly and Dunne 2017; Lemordant et al. 2018; Yang et al. 2019; Greve et al. 2019; Berg and McColl 2021; Lian et al. 2021; McColl et al. 2022). While climate models do project robust increases in VPD over land that exceed increases in precipitation, the same climate models do not exhibit obvious signs of drastic drying in relevant land surface variables, such as soil water storage or ecosystem productivity. The most common explanation for this discrepancy [termed the "aridity paradox" in Roderick et al. (2015)] is increases in plant water-use efficiency with increases in CO_2 concentrations. In a world with greater CO_2 concentrations, plants transpire less, all else being equal, meaning PET increases less rapidly with greenhouse warming than implied by increases in VPD. Since increases in PET estimated using the Penman–Monteith equation [Eq. (13)] are largely driven by increases in VPD, this also explains why aridity projections based on the Penman–Monteith equation are also unrealistically severe.

Nevertheless, there are valid reasons to be skeptical that biological plant responses to increasing CO_2 will play a first-order role in the future of the terrestrial water cycle (Vicente-Serrano et al. 2022). In addition, the aridity paradox arises in climate model simulations in which the biological plant response to increasing CO_2 is turned off (Scheff et al. 2021). This implies that plant physiological responses are, at most, only a partial explanation for the aridity paradox.

Our theory contributes to resolving the aridity paradox without invoking biological plant responses to increasing CO_2. It does so by predicting that PET should primarily scale with net radiation at large scales, rather than VPD, even in the absence of plants. To understand why, we first show a common equation for PET, obtained by taking the limit of Eq. (13) as $g_s \to \infty$:

$$\lambda \mathrm{PET} = \frac{\epsilon R_n + \rho \lambda g_a \overbrace{q^*(T_a)(1 - \mathrm{RH})}^{\mathrm{VPD}}}{\epsilon + 1} \quad \text{(incorrect!)}. \tag{19}$$

This equation includes VPD in the numerator, which increases rapidly with warming, and is the ultimate cause of large projected increases in aridity with warming. However, this equation is an incorrect measure of PET because it does not include an important land–atmosphere feedback, discussed in previous sections: A wetter surface (with higher EF) causes higher RH and lower VPD, which reduces PET. For example, in the Sahara Desert, VPD is typically very large, meaning Eq. (19) implies a very large PET. But, if the Sahara Desert was actually flooded with water—which is the hypothetical scenario relevant to PET—VPD would decline substantially from its observed value in response to land–atmosphere feedbacks

(Gallagher and McColl 2025). Equation (19) incorrectly uses the observed VPD in a given environment rather than the lower value it would take if the surface was saturated, which substantially overestimates PET (Roderick et al. 2015; Milly and Dunne 2016; Berg and McColl 2021; Kim et al. 2023; Zhou and Yu 2024). This is seen in Fig. 9c, where the Penman–Monteith estimate over a saturated surface with observed RH = 0.5 (dashed line) substantially overestimates the true value (solid black line), especially for warmer temperatures.

This problem is avoided if Eq. (14)—which includes relevant land–atmosphere feedbacks—is used instead of the Penman–Monteith equation. Taking the limit of Eq. (14) as $g_s \to \infty$ results in

$$\lambda \mathrm{PET} = R_n \frac{\epsilon + \rho \lambda g_a q^*(T_a)/R_n}{\epsilon + \rho \lambda g_a q^*(T_a)/R_n + 1}. \tag{20}$$

[This equation is equivalent to Eq. (17), but is included here for easy comparison to the Penman–Monteith PET equation.] As noted in section 5a, the term multiplying R_n on the right-hand side is only weakly sensitive to temperature for typical Earth-like conditions (Fig. 9c). This implies that PET scales primarily with net radiation, not temperature or VPD.

Why does this matter for the aridity paradox? As shown in Fig. 1 of Greve et al. (2019), if PET scales with net radiation, the aridity paradox essentially disappears, at least in the global land mean. Prior studies have shown empirically that evapotranspiration from a saturated surface primarily scales with net radiation in daily eddy–covariance observations (Maes et al. 2019) and in climate model simulations of historical and future climates (Milly and Dunne 2016; Yang et al. 2019), both with and without the biological plant response to increasing CO_2 (Milly and Dunne 2016). Our theory provides a clear mechanism for this empirically supported scaling: Wet surfaces cause high relative humidity, which causes net radiation to be the dominant driver of evapotranspiration over wet surfaces (i.e., PET). Both Kim et al. (2023) and Zhou and Yu (2024) arrive at a similar conclusion, although they invoke rather different mechanisms.

There is, of course, room for a more nuanced picture at smaller local or regional scales, or at high latitudes, for which the land and atmosphere may be less tightly coupled. However, alternative mechanisms exist at smaller scales that also suggest a wet surface will cause a wet atmosphere (Bouchet 1963; Morton 1969; Brutsaert and Stricker 1979; McColl et al. 2019b; McColl and Rigden 2020; Chen et al. 2021; Kim et al. 2023), so it is not obvious that these conclusions fail at smaller scales.

7. Conclusions

We have presented a simple theory for radiative–convective equilibrium over land surfaces with fixed soil moisture, a logical addition to the land climate model hierarchy. While most land on Earth does not have fixed soil moisture, groundwater storages act as important sources or sinks of water in many regions and can essentially fix soil moisture at high or low values, regardless of rainfall. In addition, the concept of "aridity" is based, in part, on the evapotranspiration that would arise if an unsaturated land surface was hypothetically saturated (PET). Resolving the debate about how aridity will change with warming requires understanding climates in which soil moisture is fixed.

Building on prior theory (Robinson and Catling 2012), our theory adds a (possibly dry) land surface and an interactive hydrological cycle (section 2). Our theory incorporates an expression for near-surface relative humidity from McColl and Tang (2024), which is essential to the theory's predictions of precipitation, and distinguishes it from the most similar previous literature. The simple theory is able to reproduce major aspects of cloud-permitting simulations conducted over a wide range of climates (section 3). In a special case of some relevance to Earth (the strongly mixed limit, section 4), a further simplified version of the theory results in analytic solutions.

The analytic theory is then used to understand hydrological sensitivity over saturated and unsaturated surfaces in RCE (section 5). Over sufficiently warm saturated surfaces, the theory shows that precipitation follows a radiative scaling, in which precipitation is primarily determined by atmospheric radiative cooling (or, equivalently in RCE, surface net radiation). While this result is well known, we show directly how this scaling arises from the surface energy budget, which has not been shown before. Changes in near-surface relative humidity play a critical role, and the theory of McColl and Tang (2024) is essential to this explanation. Over dry surfaces, the theory shows that precipitation follows Clausius–Clapeyron scaling, significantly larger than the typical value of 2%–3% K^{-1}. This result deepens our understanding of land climate but does not directly translate to dry land surfaces on Earth, because most land surfaces on Earth are not fixed at low soil saturation and because neglected changes in moisture flux convergence may be important.

Finally, our theory shows that the aridity paradox is at least partly an artifact caused by neglecting land–atmosphere coupling in the definition of PET (section 6). Various definitions of PET exist, but all broadly aim to provide an estimate of the amount of evapotranspiration that would occur from an environment if it was saturated. Differences in PET equations arise for a variety of reasons, particularly due to differences in which aspects of the environment are assumed fixed, rather than interactively responding to surface saturation. If it is assumed that saturating the land surface has no impact on the near-surface atmosphere, the estimated PET will be much larger than if PET is estimated using a formulation that accounts for land surface feedbacks on the atmosphere. Our formulation permits the land and atmosphere to be coupled: In particular, a wet land surface causes a wet near-surface atmosphere. This is in contrast to previous studies emphasizing the saturation vapor pressure deficit, which use a variant of the Penman–Monteith equation for a saturated surface. That equation treats the surface as saturated but does not include the response of RH to surface saturation in its definition. At sufficiently large spatial scales, relevant to global change, a truly saturated surface imposes a high near-surface relative humidity. An approximately radiative scaling can be recovered using the Penman–Monteith equation for a saturated surface if the response of RH to surface saturation is included in its definition. The radiative scaling for PET has been shown to be empirically successful but has lacked theoretical justification until now. Prior work has shown that using the radiative scaling

to estimate PET eliminates the aridity paradox (Greve et al. 2019). Our explanation is notable because it does not rely on uncertain plant physiological responses to CO_2 that are essential to prior attempts to resolve the aridity paradox.

We conclude by noting several promising directions for future research. The theory could be potentially improved by replacing the gray radiative transfer scheme with newer spectral approaches that are still simple enough to permit basic physical insight (Wilson and Gea-Banacloche 2012; Jeevanjee and Fueglistaler 2020b,a; Stevens and Kluft 2023; Koll et al. 2023). Our RCE theory neglects atmospheric moist static energy flux divergence, which is typically smaller than other terms in the atmospheric energy budget over land when averaged over sufficiently large spatial and temporal scales and outside high latitudes (Miyawaki et al. 2022). A deeper understanding of the smallest spatial and temporal scales for which this approximation is justified would improve our understanding of the theory's bounds of applicability. Atmospheric flux convergence terms could be added to the theory, if necessary, potentially with parsimonious schemes used in earlier simple models of land climate (Lintner et al. 2013). It may also be interesting to better understand the impact of heterogeneous land cover on our findings, which can induce nontrivial mesoscale circulations (Wang et al. 2000; Cheng et al. 2021, 2023; Cheng and McColl 2023, 2024). Building on Hohenegger and Stevens (2018), a natural next step would be developing a basic theory for RCE over land surfaces with interactive soil moisture and, more generally, to understand the most essential mechanisms that determine soil moisture in present and future climates (Stahl and McColl 2022; Gallagher and McColl 2025).

Acknowledgments. K. A. M. acknowledges funding from NSF Grant AGS-2129576 and a Sloan Research Fellowship. We thank Marat Khairoutdinov for providing SAM; Nick Lutsko for providing code for estimating precipitation reevaporation from SAM outputs; Yu Cheng for assistance in running the simulations; and Giuseppe Torri and Zhiming Kuang for useful conversations. We also thank Timothy W. Cronin, Benjamin Lintner, and a third reviewer for constructive reviews. The computations in this paper were run on the FASRC Cannon cluster supported by the FAS Division of Science Research Computing Group at Harvard University.

Data availability statement. The datasets generated for this study are available from the corresponding authors on request.

APPENDIX

Three Extreme Limiting Cases

For completeness, in this appendix, we consider three extreme limiting cases, corresponding to conditions that are very far from those of the modern Earth. Our theory fails in these cases. The primary focus of this work is on conditions typical of the modern Earth.

First, in the strong greenhouse limit ($\tau_0 \to \infty$), surface temperatures diverge to infinity. Shortwave radiative transfer plays a highly significant role in determining hydrological sensitivity in hothouse climates (Jeevanjee and Romps 2018; Liu et al. 2024). Since our theory does not include shortwave radiative transfer, we do not expect it to be accurate in this limit, among other reasons.

Second, in the thin atmosphere limit ($\tau_0 \to 0$), the governing equations can be simplified by noting that in Eq. (9), $e^{-\tau'}$ is approximately 1. Therefore, in the limit of $\tau_0 \to 0$, Eq. (9) simplifies to

$$F_*^{\mathrm{net}}(\tau_0) \approx \sigma T_s^4 + \sigma T_a^4 \int_0^{\tau_0} \left(\frac{\tau'}{\tau_0}\right)^{(4\beta)/n} d\tau' = \sigma T_s^4 + \sigma T_a^4 \frac{\tau_0}{\frac{4\beta}{n}+1} \to \sigma T_s^4. \tag{A1}$$

Using similar arguments, the right-hand side of Eq. (10) reduces to $F_*^{\mathrm{net}}(\tau_0) - \sigma T_s^4$, which is zero based on the previous result. Thus, Eq. (10) implies that the sum of the sensible and latent heat fluxes is zero. This will require a stably stratified layer ($T_s < T_a$), the magnitude of which will depend on the conductances and relative humidity [see Chapter 6 of Pierrehumbert (2010) for further discussion]. Our theory fails in this limit because it links the evaporative fraction (EF) to RH [Eq. (7)]. In this case, the sum of the surface turbulent fluxes is zero, the EF is infinite, and the theory predicts infinite RH, which is not physical.

Third, in the laminar limit ($g_a = 0$), there are also no surface turbulent fluxes, and surface temperatures are determined entirely by radiative transfer. This case is not equivalent to radiative equilibrium (Manabe and Strickler 1964; Manabe and Wetherald 1967; Weaver and Ramanathan 1995; Robinson and Catling 2012), since the temperature profile is prescribed by Eq. (2), rather than a solution of the governing equations. While analytic solutions for T_s and T_a are possible for this case, we do not present them because our theory fails in this limit, for the same reasons as for the thin atmosphere limit.

REFERENCES

Abbott, T. H., and T. W. Cronin, 2023: Multiple equilibria and soil moisture-precipitation feedbacks in idealized convection-permitting simulations with an open hydrological cycle. *J. Adv. Model. Earth Syst.*, **15**, e2023MS003719, https://doi.org/10.1029/2023MS003719.

Allan, R. P., and Coauthors, 2020: Advances in understanding large-scale responses of the water cycle to climate change. *Ann. N. Y. Acad. Sci.*, **1472**, 49–75, https://doi.org/10.1111/nyas.14337.

Allen, M. R., and W. J. Ingram, 2002: Constraints on future changes in climate and the hydrologic cycle. *Nature*, **419**, 224–232, https://doi.org/10.1038/nature01092.

Andrews, T., P. M. Forster, and J. M. Gregory, 2009: A surface energy perspective on climate change. *J. Climate*, **22**, 2557–2570, https://doi.org/10.1175/2008JCLI2759.1.

——, ——, O. Boucher, N. Bellouin, and A. Jones, 2010: Precipitation, radiative forcing and global temperature change. *Geophys. Res. Lett.*, **37**, L14701, https://doi.org/10.1029/2010GL043991.

Ball, J., 1933: The Qattara depression of the Libyan desert and the possibility of its utilization for power-production. *Geogr. J.*, **82**, 289–314, https://doi.org/10.2307/1785898.

Becker, T., and B. Stevens, 2014: Climate and climate sensitivity to changing CO_2 on an idealized land planet. *J. Adv. Model. Earth Syst.*, **6**, 1205–1223, https://doi.org/10.1002/2014MS000369.

Berg, A., and K. A. McColl, 2021: No projected global drylands expansion under greenhouse warming. *Nat. Climate Change*, **11**, 331–337, https://doi.org/10.1038/s41558-021-01007-8.

Beucler, T., and T. W. Cronin, 2016: Moisture-radiative cooling instability. *J. Adv. Model. Earth Syst.*, **8**, 1620–1640, https://doi.org/10.1002/2016MS000763.

Boer, G. J., 1993: Climate change and the regulation of the surface moisture and energy budgets. *Climate Dyn.*, **8**, 225–239, https://doi.org/10.1007/BF00198617.

Bonan, D. B., T. Schneider, and J. Zhu, 2024: Precipitation over a wide range of climates simulated with comprehensive GCMs. *Geophys. Res. Lett.*, **51**, e2024GL109892, https://doi.org/10.1029/2024GL109892.

Bouchet, R. J., 1963: Evapotranspiration reelle, evapotranspiration potentielle, et production agricole. *Ann. Agron.*, **14**, 743–824.

Bretherton, C. S., P. N. Blossey, and M. Khairoutdinov, 2005: An energy-balance analysis of deep convective self-aggregation above uniform SST. *J. Atmos. Sci.*, **62**, 4273–4292, https://doi.org/10.1175/JAS3614.1.

Brutsaert, W., and H. Stricker, 1979: An advection-aridity approach to estimate actual regional evapotranspiration. *Water Resour. Res.*, **15**, 443–450, https://doi.org/10.1029/WR015i002p00443.

Budyko, M. I., 1958: The heat balance of the Earth's surface. NWS, US Department of Commerce Tech. Rep., 134 pp., https://mghydro.com/wp-content/uploads/2025/01/Budyko-1956-1.pdf.

Chen, J., and Coauthors, 2022: Response of surface evaporation and subsurface leakage to precipitation for simulated epikarst with different rock–soil structures. *J. Hydrol.*, **610**, 127850, https://doi.org/10.1016/j.jhydrol.2022.127850.

Chen, S., K. A. McColl, A. Berg, and Y. Huang, 2021: Surface flux equilibrium estimates of evapotranspiration at large spatial scales. *J. Hydrometeor.*, **22**, 765–779, https://doi.org/10.1175/JHM-D-20-0204.1.

Cheng, Y., and K. A. McColl, 2023: Thermally direct mesoscale circulations caused by land surface roughness anomalies. *Geophys. Res. Lett.*, **50**, e2023GL105150, https://doi.org/10.1029/2023GL105150.

——, and ——, 2024: Unexpected warming from land radiative management. *Geophys. Res. Lett.*, **51**, e2024GL112433, https://doi.org/10.1029/2024GL112433.

——, P. W. Chan, X. Wei, Z. Hu, Z. Kuang, and K. A. McColl, 2021: Soil moisture control of precipitation reevaporation over a heterogeneous land surface. *J. Atmos. Sci.*, **78**, 3369–3383, https://doi.org/10.1175/JAS-D-21-0059.1.

——, Z. Hu, and K. A. McColl, 2023: Anomalously darker land surfaces become wetter due to mesoscale circulations. *Geophys. Res. Lett.*, **50**, e2023GL104137, https://doi.org/10.1029/2023GL104137.

Cronin, T. W., and D. R. Chavas, 2019: Dry and semidry tropical cyclones. *J. Atmos. Sci.*, **76**, 2193–2212, https://doi.org/10.1175/JAS-D-18-0357.1.

——, K. A. Emanuel, and P. Molnar, 2015: Island precipitation enhancement and the diurnal cycle in radiative-convective equilibrium. *Quart. J. Roy. Meteor. Soc.*, **141**, 1017–1034, https://doi.org/10.1002/qj.2443.

Dagan, G., and P. Stier, 2020: Constraint on precipitation response to climate change by combination of atmospheric energy and water budgets. *npj Climate Atmos. Sci.*, **3**, 34, https://doi.org/10.1038/s41612-020-00137-8.

——, and E. Eytan, 2024: The potential of absorbing aerosols to enhance extreme precipitation. *Geophys. Res. Lett.*, **51**, e2024GL108385, https://doi.org/10.1029/2024GL108385.

Delworth, T., and S. Manabe, 1989: The influence of soil wetness on near-surface atmospheric variability. *J. Climate*, **2**, 1447–1462, https://doi.org/10.1175/1520-0442(1989)002<1447:TIOSWO>2.0.CO;2.

Embabi, N. S., 2018: The Qattara depression. *Landscapes and Landforms of Egypt: Landforms and Evolution*, N. S. Embabi, Ed., Springer International Publishing, 121–132, https://doi.org/10.1007/978-3-319-65661-8_10.

Field, C. B., R. B. Jackson, and H. A. Mooney, 1995: Stomatal responses to increased CO_2: Implications from the plant to the global scale. *Plant Cell Environ.*, **18**, 1214–1225, https://doi.org/10.1111/j.1365-3040.1995.tb00630.x.

Gallagher, T., and K. A. McColl, 2025: Climate-scale variability in soil moisture explained by a simple theory. *Geophys. Res. Lett.*, **52**, e2025GL115044, https://doi.org/10.1029/2025GL115044.

Greve, P., M. L. Roderick, A. M. Ukkola, and Y. Wada, 2019: The aridity index under global warming. *Environ. Res. Lett.*, **14**, 124006, https://doi.org/10.1088/1748-9326/ab5046.

Hartmann, D. L., and K. Larson, 2002: An important constraint on tropical cloud - climate feedback. *Geophys. Res. Lett.*, **29**, 1951, https://doi.org/10.1029/2002GL015835.

Held, I. M., 2005: The gap between simulation and understanding in climate modeling. *Bull. Amer. Meteor. Soc.*, **86**, 1609–1614, https://doi.org/10.1175/BAMS-86-11-1609.

Hohenegger, C., and B. Stevens, 2016: Coupled radiative convective equilibrium simulations with explicit and parameterized convection. *J. Adv. Model. Earth Syst.*, **8**, 1468–1482, https://doi.org/10.1002/2016MS000666.

——, and ——, 2018: The role of the permanent wilting point in controlling the spatial distribution of precipitation. *Proc. Natl. Acad. Sci. USA*, **115**, 5692–5697, https://doi.org/10.1073/pnas.1718842115.

Hörst, S. M., 2017: Titan's atmosphere and climate. *J. Geophys. Res. Planets*, **122**, 432–482, https://doi.org/10.1002/2016JE005240.

Jakob, C., M. S. Singh, and L. Jungandreas, 2019: Radiative convective equilibrium and organized convection: An observational perspective. *J. Geophys. Res. Atmos.*, **124**, 5418–5430, https://doi.org/10.1029/2018JD030092.

Jeevanjee, N., and D. M. Romps, 2018: Mean precipitation change from a deepening troposphere. *Proc. Natl. Acad. Sci. USA*, **115**, 11 465–11 470, https://doi.org/10.1073/pnas.1720683115.

——, and S. Fueglistaler, 2020a: On the cooling-to-space approximation. *J. Atmos. Sci.*, **77**, 465–478, https://doi.org/10.1175/JAS-D-18-0352.1.

——, and ——, 2020b: Simple spectral models for atmospheric radiative cooling. *J. Atmos. Sci.*, **77**, 479–497, https://doi.org/10.1175/JAS-D-18-0347.1.

——, P. Hassanzadeh, S. Hill, and A. Sheshadri, 2017: A perspective on climate model hierarchies. *J. Adv. Model. Earth Syst.*, **9**, 1760–1771, https://doi.org/10.1002/2017MS001038.

——, I. Held, and V. Ramaswamy, 2022: Manabe's radiative–convective equilibrium. *Bull. Amer. Meteor. Soc.*, **103**, E2559–E2569, https://doi.org/10.1175/BAMS-D-21-0351.1.

Khairoutdinov, M. F., and D. A. Randall, 2003: Cloud resolving modeling of the ARM summer 1997 IOP: Model formulation, results, uncertainties, and sensitivities. *J. Atmos. Sci.*, **60**, 607–625, https://doi.org/10.1175/1520-0469(2003)060<0607:CRMOTA>2.0.CO;2.

Kim, Y., M. Garcia, and M. S. Johnson, 2023: Land-atmosphere coupling constrains increases to potential evaporation in a warming

climate: Implications at local and global scales. *Earth's Future*, **11**, e2022EF002886, https://doi.org/10.1029/2022EF002886.

Kleidon, A., and M. Renner, 2013: A simple explanation for the sensitivity of the hydrologic cycle to surface temperature and solar radiation and its implications for global climate change. *Earth Syst. Dyn.*, **4**, 455–465, https://doi.org/10.5194/esd-4-455-2013.

Koll, D. D. B., N. Jeevanjee, and N. J. Lutsko, 2023: An analytic model for the clear-sky longwave feedback. *J. Atmos. Sci.*, **80**, 1923–1951, https://doi.org/10.1175/JAS-D-22-0178.1.

Laio, F., S. Tamea, L. Ridolfi, P. D'Odorico, and I. Rodriguez-Iturbe, 2009: Ecohydrology of groundwater-dependent ecosystems: 1. Stochastic water table dynamics. *Water Resour. Res.*, **45**, W05419, https://doi.org/10.1029/2008WR007292.

Lee, J. M., and M. Khairoutdinov, 2015: A Simplified Land Model (SLM) for use in cloud-resolving models: Formulation and evaluation. *J. Adv. Model. Earth Syst.*, **7**, 1368–1392, https://doi.org/10.1002/2014MS000419.

Lemordant, L., P. Gentine, A. S. Swann, B. I. Cook, and J. Scheff, 2018: Critical impact of vegetation physiology on the continental hydrologic cycle in response to increasing CO_2. *Proc. Natl. Acad. Sci.*, **115**, 4093–4098, https://doi.org/10.1073/pnas.1720712115.

Leutwyler, D., and C. Hohenegger, 2021: Weak cooling of the troposphere by tropical islands in simulations of the radiative-convective equilibrium. *Quart. J. Roy. Meteor. Soc.*, **147**, 1788–1800, https://doi.org/10.1002/qj.3995.

Lian, X., and Coauthors, 2021: Multifaceted characteristics of dryland aridity changes in a warming world. *Nat. Rev. Earth Environ.*, **2**, 232–250, https://doi.org/10.1038/s43017-021-00144-0.

Lintner, B. R., P. Gentine, K. L. Findell, F. D'Andrea, A. H. Sobel, and G. D. Salvucci, 2013: An idealized prototype for large-scale land–atmosphere coupling. *J. Climate*, **26**, 2379–2389, https://doi.org/10.1175/JCLI-D-11-00561.1.

Liu, J., J. Yang, F. Ding, G. Chen, and Y. Hu, 2024: Hydrologic cycle weakening in hothouse climates. *Sci. Adv.*, **10**, eado2515, https://doi.org/10.1126/sciadv.ado2515.

Lorenz, D. J., E. T. DeWeaver, and D. J. Vimont, 2010: Evaporation change and global warming: The role of net radiation and relative humidity. *J. Geophys. Res.*, **115**, D20118, https://doi.org/10.1029/2010JD013949.

Maes, W. H., P. Gentine, N. E. C. Verhoest, and D. G. Miralles, 2019: Potential evaporation at eddy-covariance sites across the globe. *Hydrol. Earth Syst. Sci.*, **23**, 925–948, https://doi.org/10.5194/hess-23-925-2019.

Maher, P., and Coauthors, 2019: Model hierarchies for understanding atmospheric circulation. *Rev. Geophys.*, **57**, 250–280, https://doi.org/10.1029/2018RG000607.

Manabe, S., and R. F. Strickler, 1964: Thermal equilibrium of the atmosphere with a convective adjustment. *J. Atmos. Sci.*, **21**, 361–385, https://doi.org/10.1175/1520-0469(1964)021<0361:TEOTAW>2.0.CO;2.

——, and R. T. Wetherald, 1967: Thermal equilibrium of the atmosphere with a given distribution of relative humidity. *J. Atmos. Sci.*, **24**, 241–259, https://doi.org/10.1175/1520-0469(1967)024<0241:TEOTAW>2.0.CO;2.

McColl, K. A., 2020: Practical and theoretical benefits of an alternative to the Penman-Monteith evapotranspiration equation. *Water Resour. Res.*, **56**, e2020WR027106, https://doi.org/10.1029/2020WR027106.

——, and A. J. Rigden, 2020: Emergent simplicity of continental evapotranspiration. *Geophys. Res. Lett.*, **47**, e2020GL087101, https://doi.org/10.1029/2020GL087101.

——, and L. I. Tang, 2024: An analytic theory of near-surface relative humidity over land. *J. Climate*, **37**, 1213–1230, https://doi.org/10.1175/JCLI-D-23-0342.1.

——, W. Wang, B. Peng, R. Akbar, D. J. Short Gianotti, H. Lu, M. Pan, and D. Entekhabi, 2017: Global characterization of surface soil moisture drydowns. *Geophys. Res. Lett.*, **44**, 3682–3690, https://doi.org/10.1002/2017GL072819.

——, Q. He, H. Lu, and D. Entekhabi, 2019a: Short-term and long-term surface soil moisture memory time scales are spatially anticorrelated at global scales. *J. Hydrometeor.*, **20**, 1165–1182, https://doi.org/10.1175/JHM-D-18-0141.1.

——, G. D. Salvucci, and P. Gentine, 2019b: Surface flux equilibrium theory explains an empirical estimate of water-limited daily evapotranspiration. *J. Adv. Model. Earth Syst.*, **11**, 2036–2049, https://doi.org/10.1029/2019MS001685.

——, M. L. Roderick, A. Berg, and J. Scheff, 2022: The terrestrial water cycle in a warming world. *Nat. Climate Change*, **12**, 604–606, https://doi.org/10.1038/s41558-022-01412-7.

Milly, P. C. D., and K. A. Dunne, 2016: Potential evapotranspiration and continental drying. *Nat. Climate Change*, **6**, 946–949, https://doi.org/10.1038/nclimate3046.

——, and ——, 2017: A hydrologic drying bias in water-resource impact analyses of anthropogenic climate change. *J. Amer. Water Resour. Assoc.*, **53**, 822–838, https://doi.org/10.1111/1752-1688.12538.

Mitchell, J. F. B., C. A. Wilson, and W. M. Cunnington, 1987: On Co^2 climate sensitivity and model dependence of results. *Quart. J. Roy. Meteor. Soc.*, **113**, 293–322, https://doi.org/10.1256/smsqj.47516.

Miyawaki, O., T. A. Shaw, and M. F. Jansen, 2022: Quantifying energy balance regimes in the modern climate, their link to lapse rate regimes, and their response to warming. *J. Climate*, **35**, 1045–1061, https://doi.org/10.1175/JCLI-D-21-0440.1.

Monteith, J., 1965: Evaporation and environment. *The State and Movement of Water in Living Organisms.* Cambridge University Press, 205–234.

Morton, F. I., 1969: Potential evaporation as a manifestation of regional evaporation. *Water Resour. Res.*, **5**, 1244–1255, https://doi.org/10.1029/WR005i006p01244.

O'Gorman, P. A., and T. Schneider, 2008: The hydrological cycle over a wide range of climates simulated with an idealized GCM. *J. Climate*, **21**, 3815–3832, https://doi.org/10.1175/2007JCLI2065.1.

——, R. P. Allan, M. P. Byrne, and M. Previdi, 2012: Energetic constraints on precipitation under climate change. *Surv. Geophys.*, **33**, 585–608, https://doi.org/10.1007/s10712-011-9159-6.

Pendergrass, A. G., and D. L. Hartmann, 2014: The atmospheric energy constraint on global-mean precipitation change. *J. Climate*, **27**, 757–768, https://doi.org/10.1175/JCLI-D-13-00163.1.

Penman, H. L., 1948: Natural evaporation from open water, bare soil and grass. *Proc. Roy. Soc.*, **193A**, 120–145, https://doi.org/10.1098/rspa.1948.0037.

Pierrehumbert, R. T., 2002: The hydrologic cycle in deep-time climate problems. *Nature*, **419**, 191–198, https://doi.org/10.1038/nature01088.

——, 2010: *Principles of Planetary Climate.* Cambridge University Press, 652 pp.

Priestley, C. H. B., and R. J. Taylor, 1972: On the assessment of surface heat flux and evaporation using large-scale parameters. *Mon. Wea. Rev.*, **100**, 81–92, https://doi.org/10.1175/1520-0493(1972)100<0081:OTAOSH>2.3.CO;2.

Rahmati, M., and Coauthors, 2024: Soil moisture memory: State-of-the-art and the way forward. *Rev. Geophys.*, **62**, e2023RG000828, https://doi.org/10.1029/2023RG000828.

Ramanathan, V., and J. A. Coakley Jr., 1978: Climate modeling through radiative-convective models. *Rev. Geophys.*, **16**, 465–489, https://doi.org/10.1029/RG016i004p00465.

Raupach, M. R., 2000: Equilibrium evaporation and the convective boundary layer. *Bound.-Layer Meteor.*, **96**, 107–142, https://doi.org/10.1023/A:1002675729075.

——, 2001: Combination theory and equilibrium evaporation. *Quart. J. Roy. Meteor. Soc.*, **127**, 1149–1181, https://doi.org/10.1256/smsqj.57401.

Renno, N. O., 1997: Multiple equilibria in radiative-convective atmospheres. *Tellus*, **49A**, 423–438, https://doi.org/10.3402/tellusa.v49i4.14681.

Richter, I., and S.-P. Xie, 2008: Muted precipitation increase in global warming simulations: A surface evaporation perspective. *J. Geophys. Res.*, **113**, D24118, https://doi.org/10.1029/2008JD010561.

Robinson, T. D., and D. C. Catling, 2012: An analytic radiative–convective model for planetary atmospheres. *Astrophys. J.*, **757**, 104, https://doi.org/10.1088/0004-637X/757/1/104.

Rochetin, N., B. R. Lintner, K. L. Findell, A. H. Sobel, and P. Gentine, 2014: Radiative–convective equilibrium over a land surface. *J. Climate*, **27**, 8611–8629, https://doi.org/10.1175/JCLI-D-13-00654.1.

Roderick, M. L., P. Greve, and G. D. Farquhar, 2015: On the assessment of aridity with changes in atmospheric CO_2. *Water Resour. Res.*, **51**, 5450–5463, https://doi.org/10.1002/2015WR017031.

Rohde, M. M., and Coauthors, 2024: Groundwater-dependent ecosystem map exposes global dryland protection needs. *Nature*, **632**, 101–107, https://doi.org/10.1038/s41586-024-07702-8.

Samset, B. H., and Coauthors, 2018: Weak hydrological sensitivity to temperature change over land, independent of climate forcing. *npj Climate Atmos. Sci.*, **1**, 20173, https://doi.org/10.1038/s41612-017-0005-5.

Scheff, J., and D. M. W. Frierson, 2014: Scaling potential evapotranspiration with greenhouse warming. *J. Climate*, **27**, 1539–1558, https://doi.org/10.1175/JCLI-D-13-00233.1.

——, and ——, 2015: Terrestrial aridity and its response to greenhouse warming across CMIP5 climate models. *J. Climate*, **28**, 5583–5600, https://doi.org/10.1175/JCLI-D-14-00480.1.

——, J. S. Mankin, S. Coats, and H. Liu, 2021: CO_2-plant effects do not account for the gap between dryness indices and projected dryness impacts in CMIP6 or CMIP5. *Environ. Res. Lett.*, **16**, 034018, https://doi.org/10.1088/1748-9326/abd8fd.

Schneider, T., C. M. Kaul, and K. G. Pressel, 2019: Possible climate transitions from breakup of stratocumulus decks under greenhouse warming. *Nat. Geosci.*, **12**, 163–167, https://doi.org/10.1038/s41561-019-0310-1.

Seeley, J. T., and R. D. Wordsworth, 2021: Episodic deluges in simulated hothouse climates. *Nature*, **599**, 74–79, https://doi.org/10.1038/s41586-021-03919-z.

——, N. Jeevanjee, and D. M. Romps, 2019: FAT or FiTT: Are anvil clouds or the tropopause temperature invariant? *Geophys. Res. Lett.*, **46**, 1842–1850, https://doi.org/10.1029/2018GL080096.

Sherwood, S., and Q. Fu, 2014: A drier future? *Science*, **343**, 737–739, https://doi.org/10.1126/science.1247620.

Siler, N., G. H. Roe, K. C. Armour, and N. Feldl, 2019: Revisiting the surface-energy-flux perspective on the sensitivity of global precipitation to climate change. *Climate Dyn.*, **52**, 3983–3995, https://doi.org/10.1007/s00382-018-4359-0.

Singh, M. S., and M. E. O'Neill, 2022: The climate system and the second law of thermodynamics. *Rev. Mod. Phys.*, **94**, 015001, https://doi.org/10.1103/RevModPhys.94.015001.

Slatyer, R. O., and I. McIlroy, 1961: *Practical Microclimatology: With Special Reference to the Water Factor in Soil-Plant-Atmosphere Relationships*. Commonwealth Scientific and Industrial Research Organisation, 337 pp.

Stahl, M. O., and K. A. McColl, 2022: The seasonal cycle of surface soil moisture. *J. Climate*, **35**, 4997–5012, https://doi.org/10.1175/JCLI-D-21-0780.1.

Stevens, B., and L. Kluft, 2023: A colorful look at climate sensitivity. *Atmos. Chem. Phys.*, **23**, 14 673–14 689, https://doi.org/10.5194/acp-23-14673-2023.

Swann, A. L. S., F. M. Hoffman, C. D. Koven, and J. T. Randerson, 2016: Plant responses to increasing CO_2 reduce estimates of climate impacts on drought severity. *Proc. Natl. Acad. Sci. USA*, **113**, 10 019–10 024, https://doi.org/10.1073/pnas.1604581113.

Takahashi, K., 2009: Radiative constraints on the hydrological cycle in an idealized radiative–convective equilibrium model. *J. Atmos. Sci.*, **66**, 77–91, https://doi.org/10.1175/2008JAS2797.1.

Tamea, S., F. Laio, L. Ridolfi, P. D'Odorico, and I. Rodriguez-Iturbe, 2009: Ecohydrology of groundwater-dependent ecosystems: 2. Stochastic soil moisture dynamics. *Water Resour. Res.*, **45**, W05420, https://doi.org/10.1029/2008WR007293.

Tan, Z., T. Schneider, J. Teixeira, and K. G. Pressel, 2016: Large-eddy simulation of subtropical cloud-topped boundary layers: 1. A forcing framework with closed surface energy balance. *J. Adv. Model. Earth Syst.*, **8**, 1565–1585, https://doi.org/10.1002/2016MS000655.

Tompkins, A. M., and G. C. Craig, 1998: Radiative–convective equilibrium in a three-dimensional cloud-ensemble model. *Quart. J. Roy. Meteor. Soc.*, **124**, 2073–2097, https://doi.org/10.1256/smsqj.55012.

Vicente-Serrano, S. M., D. G. Miralles, N. McDowell, T. Brodribb, F. Domínguez-Castro, R. Leung, and A. Koppa, 2022: The uncertain role of rising atmospheric CO_2 on global plant transpiration. *Earth. Sci. Rev.*, **230**, 104055, https://doi.org/10.1016/j.earscirev.2022.104055.

Voss, C. I., and S. M. Soliman, 2014: The transboundary nonrenewable Nubian aquifer system of Chad, Egypt, Libya and Sudan: Classical groundwater questions and parsimonious hydrogeologic analysis and modeling. *Hydrogeol. J.*, **22**, 441–468, https://doi.org/10.1007/s10040-013-1039-3.

Wang, J., R. L. Bras, and E. A. B. Eltahir, 2000: The impact of observed deforestation on the mesoscale distribution of rainfall and clouds in Amazonia. *J. Hydrometeor.*, **1**, 267–286, https://doi.org/10.1175/1525-7541(2000)001<0267:TIOODO>2.0.CO;2.

Wang, W., T. C. Chakraborty, W. Xiao, and X. Lee, 2021: Ocean surface energy balance allows a constraint on the sensitivity of precipitation to global warming. *Nat. Commun.*, **12**, 2115, https://doi.org/10.1038/s41467-021-22406-7.

Weaver, C. P., and V. Ramanathan, 1995: Deductions from a simple climate model: Factors governing surface temperature and atmospheric thermal structure. *J. Geophys. Res.*, **100**, 11 585–11 591, https://doi.org/10.1029/95JD00770.

Wilson, D. J., and J. Gea-Banacloche, 2012: Simple model to estimate the contribution of atmospheric CO_2 to the Earth's greenhouse effect. *Amer. J. Phys.*, **80**, 306–315, https://doi.org/10.1119/1.3681188.

Wing, A. A., K. A. Reed, M. Satoh, B. Stevens, S. Bony, and T. Ohno, 2018: Radiative–convective equilibrium model intercomparison project. *Geosci. Model Dev.*, **11**, 793–813, https://doi.org/10.5194/gmd-11-793-2018.

Yang, Y., M. L. Roderick, S. Zhang, T. R. McVicar, and R. J. Donohue, 2019: Hydrologic implications of vegetation response to elevated CO_2 in climate projections. *Nat. Climate Change*, **9**, 44–48, https://doi.org/10.1038/s41558-018-0361-0.

Zhou, S., and B. Yu, 2024: Physical basis of the potential evapotranspiration and its estimation over land. *J. Hydrol.*, **641**, 131825, https://doi.org/10.1016/j.jhydrol.2024.131825.

Zhou, W., L. R. Leung, and J. Lu, 2023: The role of interactive soil moisture in land drying under anthropogenic warming. *Geophys. Res. Lett.*, **50**, e2023GL105308, https://doi.org/10.1029/2023GL105308.